Improving High-Resolution Numerical Weather Simulations by Assimilating Data from an Unmanned Aerial System

Marius O. Jonassen

University of Bergen, Bergen, Norway

Haraldur Ólafsson

University of Bergen, Bergen, Norway, and Department of Physics, University of Iceland, Icelandic Meteorological Office, Reykjavik, Iceland

Hálfdán Ágústsson

Department of Physics, University of Iceland, and Institute for Meteorological Research, Reykjavik, Iceland

Ólafur Rögnvaldsson

University of Bergen, Bergen, Norway, and Institute for Meteorological Research, Reykjavik, Iceland

Joachim Reuder

University of Bergen, Bergen, Norway

(Manuscript received 30 November 2011, in final form 23 April 2012)

ABSTRACT

In this study, it is demonstrated how temperature, humidity, and wind profile data from the lower troposphere obtained with a lightweight unmanned aerial system (UAS) can be used to improve high-resolution numerical weather simulations by four-dimensional data assimilation (FDDA). The combined UAS and FDDA system is applied to two case studies of northeasterly flow situations in southwest Iceland from the international Moso field campaign on 19 and 20 July 2009. Both situations were characterized by high diurnal boundary layer temperature variation leading to thermally driven flow, predominantly in the form of sea-breeze circulation along the coast. The data assimilation leads to an improvement in the simulation of the horizontal and vertical extension of the sea breeze as well as of the local background flow. Erroneously simulated fog over the Reykjanes peninsula on 19 July, which leads to a local temperature underestimation of 8 K, is also corrected by the data assimilation. Sensitivity experiments show that both the assimilation of wind data and temperature and humidity data are important for the assimilation results. UAS represents a novel instrument platform with a large potential within the atmospheric sciences. The presented method of using UAS data for assimilation into high-resolution numerical weather simulations is likely to have a wide range of future applications such as wind energy and improvements of targeted weather forecasts for search and rescue missions.

1. Introduction

A numerical weather model's ability to accurately simulate atmospheric dynamical and physical processes depends critically on several factors. These are among others the spatial grid resolution and the parameterization schemes used to represent processes connected to clouds, radiation, precipitation, and turbulence (e.g., Pleim and Xiu 1995; Alapaty et al. 2001; Teixeira et al. 2008). In addition, the quality of the data used to initialize and force the model is essential for the success of a numerical simulation. These data often originate from global atmospheric analyses or forecasts [e.g., from the Global Forecast System (GFS) or the European Centre for Medium-Range Weather Forecasts (ECMWF)] with resolutions typically being 15–50 km in the horizontal

and 3–6 h in time. These atmospheric data are often not accurate enough for high-resolution simulations of local features, which may be sensitive to small errors in the large-scale flow, as pointed out by Nance and Durran (1997) in their study of lee waves. The quality of the analysis data depends mainly on two factors. One is the technique used to compile the analysis (i.e., the numerical weather prediction model used to generate the first guess and the statistical methods used to combine the first-guess information and the observations). The second factor is the quality and coverage of the observations used to create the analysis (e.g., Langland et al. 1999). Observations can be particularly sparse over areas such as the world's oceans and the Arctic and Antarctic.

To improve numerical weather simulations, the initial and forcing data are often supplemented with additional in situ or remote sensing observations through a method called nudging, or four-dimensional data assimilation (FDDA; e.g., Anthes 1974; Stauffer and Seaman 1990, 1994; Stauffer et al. 1991). When applied to observational data, as done in the present study, this assimilation method "nudges" the modeled atmospheric state toward the observations by introducing an artificial forcing term in the model's governing equations. The forcing term is based on the difference between the modeled and observed atmospheric state. Compared to alternative data assimilation methods, like three/four-dimensional variational data assimilation (3D-Var or 4D-Var) and ensemble Kalman filter methods, nudging is conceptually simple and computationally inexpensive (e.g., Stauffer and Seaman 1990; Fast 1995; Reen and Stauffer 2010).

The provision of corresponding data for assimilation and also for model validation, however, poses major technical challenges. This is especially valid for high-resolution numerical simulations of the atmospheric boundary layer (ABL), as the operational network of automatic weather stations and radiosondes generally is too sparse and unevenly distributed to accurately describe the temperature, wind, and moisture structure with high temporal and spatial resolution (e.g., Otkin et al. 2011). Conventional in situ instrument platforms like towers and captive balloons and remote sensing technologies as lidars, radars, sodars, and satellites have the potential of aiding toward the desired datasets for assimilation and validation. For some applications, like meteorological field campaigns that are targeted toward specific ABL phenomena in remote areas, and that are limited in time and by a small budget, these instrument platforms may, however, be too expensive. They may furthermore be too demanding to operate in the field (e.g., due to the requirement of expert personnel, limited in-field mobility, and infrastructural requirements like a continuous demand for electricity). In this context, unmanned aerial systems (UASs) have the potential to become an invaluable tool in ABL research. These systems, consisting mainly of an unmanned aircraft and a ground control station, were for the first time used for atmospheric measurements in the 1970s (Konrad et al. 1970). Following the recent development in microelectrical components, both with respect to avionics as well as instrumentation and sensors for atmospheric measurements, these have now become significantly more viable and feature among other things fully autonomous navigation and advanced mission planning tools.

Examples of such systems include the Mini Aerial Vehicle (M^{2}AV; Van den Kroonenberg et al. 2008; Martin et al. 2010), the Aerosonde (Curry et al. 2004), and the Small Unmanned Meteorological Observer (SUMO; Reuder et al. 2009). These lightweight UASs represent a novel and very flexible instrument platform that is generally user friendly and cost efficient to operate. Furthermore, they are able to provide a unique data coverage in both space and time and thereby have the potential to augment and fill the observational gap between the aforementioned conventional instrument platforms. They are able to provide in situ data, not reliant on similarity or propagation assumptions, and they are undisturbed by clouds. Data delivery is fast or even instantaneous. Their low infrastructure requirements allow them to be used in otherwise data-sparse regions, such as the polar areas where the mentioned UASs have already been successfully operated.

In this article, we demonstrate a combined UAS and FDDA system, where profile data of temperature, humidity, and wind obtained with the UAS SUMO are assimilated into the Weather Research and Forecasting Model (WRF; Skamarock et al. 2008) using the FDDA technique. The system is applied to two case studies of weather situations that took place during the international Moso field campaign on 19 and 20 July 2009, in southwest Iceland. The weather situations were characterized by strong diurnal boundary layer temperature variation leading to thermally driven winds, predominantly in the form of sea-breeze circulation along the coast.

Sea breeze is recognized to have a great influence on the local to mesoscale flow in coastal areas. Knowledge on and predictability of this circulation may play an important role in local weather forecasting for aviation and transport at sea. Sea breeze is also found to be of large importance for the formation and movement of thunderstorm complexes (e.g., Pielke 1974) and transport of pollutants (e.g., Warner et al. 1978; Soler et al.

2011). Sea breeze is a widely studied phenomenon and reviews are given by Stull (1988) and Pielke (2002). Very few studies, however, focus on sea breeze at high latitudes. One such study is that by Grønås and Sandvik (1998) who studied sea breeze at latitudes higher than 60°N. With a main focus on Norway and Spitsbergen they found through idealized numerical simulations that the sea breeze is well developed at these latitudes in summertime. Another study of sea breeze at higher latitudes is that of Gahmberg et al. (2010) who focused on the interaction between sea breeze and synoptic flow. They found among other things the strongest sea breeze for moderate large-scale flows blowing 45°–90° anticlockwise from the offshore direction perpendicular to the coast.

Sea breeze in Iceland is mentioned in the paper of Bromwich et al. (2005), who made a high-resolution regional climate simulation of Iceland for 1991–2000. They concluded that sea breeze appears to be an integral part of the summertime weather along most of the coastline. Jónsson (2002) investigated wind speed and wind directions recorded by automatic weather stations throughout Iceland for the month of June and found observational evidence of the climatological presence of sea breeze in Iceland.

Sea-breeze circulations are finely balanced systems and typically a challenge for operational numerical weather prediction systems to accurately reproduce in both time and space (e.g., Fuentes et al. 2005). How the numerical simulations reproduce the surface and boundary layer flow and temperature including the sea-breeze circulation, with and without the assimilation of all and parts of the UAS temperature, humidity, and wind data, is the main topic of this study. In addition, several sensitivity experiments on different nudging parameters are carried out.

2. Observations

a. The Moso field campaign

The international Moso field campaign was conducted in southwest Iceland in the period from 9 to 20 July 2009. The campaign, which name is short for "Mosfellsbær," a small settlement outside Reykjavik, Iceland, was dedicated to the study of thermally driven and orographically modified mesoscale flow. In the first part of the campaign, the formation of weak gravity waves was studied using the UAS SUMO and a network of automatic weather stations in the vicinity of Reykjavik. Using the same observational tools, two weather situations dominated by sea-breeze circulation along the southwest coast of Iceland on 19 and 20 July were observed in a second part the campaign.

The present study focuses on the results from this second part, while the first part will be the subject of a future study.

The study region can be divided into an eastern and a western area as naturally separated by the Reykjanes mountain range (ca. 350–800 MSL; Fig. 1). The eastern area is the area of main interest and the UAS soundings were made at Eyrarbakki, Iceland. The central parts of the eastern region mostly consist of relatively flat, farmed land, while the outskirts of the area are dominated by more complex topography, most markedly by the Eyjafjallajökull (1666 MSL) and Myrdalsjökull (1450 MSL) massif in the southeast [north of automatic weather stations (AWSs) Steinar and Hvammur] and the Reykjanes mountain range in the west.

AWS data from the western area are included as complementary information to investigate the spatial extension of the impact of the data assimilation.

NEAR-SURFACE OBSERVATIONS: AUTOMATIC WEATHER STATIONS (AWSS)

In southwest Iceland, there is a rather dense network of AWSs, run mainly by the Icelandic Meteorological Office (Veðurstofa Íslands) and the Icelandic Road Administration (ICERA/Vegagerðin). The AWS data in this study are based on 10-min averages and obtained with a temporal resolution of 1 h. Temperature and relative humidity are measured at 2 m above the ground level and the wind is observed at 10 m or at the top of a 6-m-high mast raised approximately 1 m above its immediate surroundings (Skalholt). Most stations are located below 50 MSL.

b. Small Unmanned Meteorological Observer (SUMO)

The atmospheric profiles used in this study were made with the UAS SUMO (Reuder et al. 2009) that has been developed in a collaboration between the Geophysical Institute, University of Bergen, and Martin Müller Engineering, Germany. SUMO consists of three main parts: a small model aircraft, a ground control station, and a remote control. It is equipped with an autopilot system that is developed under the open-source Paparazzi project supervised by the French school for civil aviation, Ecole Nationale de l'Aviation Civile (ENAC; Brisset et al. 2006). In its current version, the SUMO airframe is the commercially available FunJet construction kit from Multiplex. With a weight of only 0.58 kg, a wingspan of 0.8 m, and length of 0.75 m, the airframe is relatively small and lightweight and thus ideal for use in remote areas and complex terrain with a minimum of infrastructural facilities. The system is very quickly deployed in the field and is ready for operation within
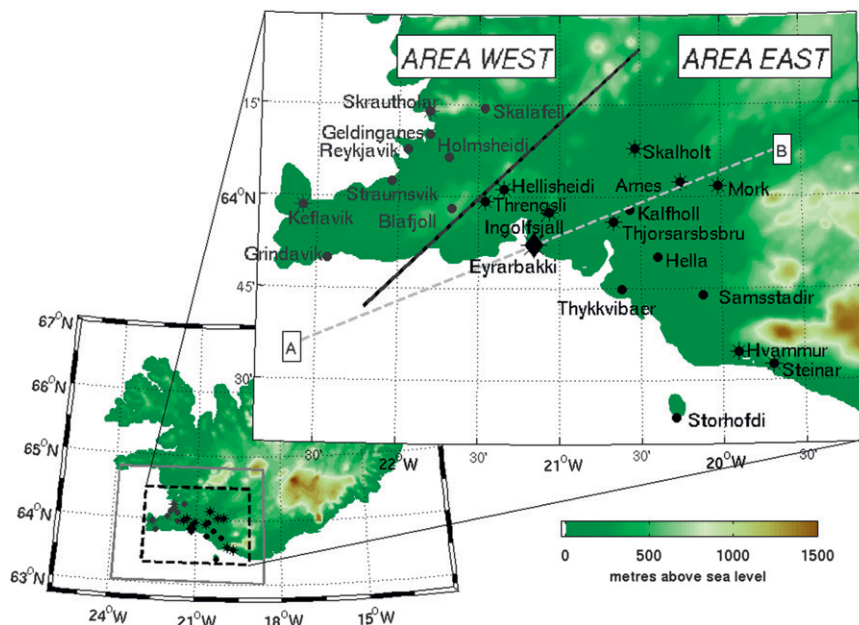
FIG. 1. (top right) Overview over the experiment area. (bottom left) The area is slightly smaller than domain 3 (gray box). The locations of the automatic weather stations are indicated by dots and names. The stations additionally marked with a star do not measure relative humidity. The main observation site for the UAS SUMO, Eyrarbakki, is marked by a diamond. The area east is the area of main interest where the studied sea-breeze events took place. The geographical division between area east and area west is indicated by a black line. The gray, dashed line (from A to B) indicates the position of the vertical cross sections of wind speed and specific humidity in Figs. 15 and 16.

10–15 min from arriving at the measurement site. The aircraft is electrically powered by lithium polymer batteries giving a typical flight endurance of 20–45 min, depending mainly on the flight pattern, wind speed, and the atmospheric temperature. Within this time frame, a maximum altitude of around 5 km can be reached. During the Moso field campaign, the system was equipped with sensors for the measurement of temperature, relative humidity, and pressure. The manufacturer (Sensirion) of the combined temperature and humidity sensor (SHT 75) gives an absolute accuracy of respectively 0.3°C and 1.8%. Wind direction and wind speed is estimated indirectly by a method relying on the onboard GPS data and an assumption of constant true-airspeed and constant pitch angle. The method is described in more detail by Mayer et al. (2012). The flight pattern used for atmospheric profiling resembles a helix that corresponds to an atmospheric column with a radius of 50–100 m. The aircraft has relatively high ascent and descent speeds (5–8 m s^{-1}) and because of a relatively slow sensor response, the temperature and humidity data have been corrected using a method outlined in Jonassen (2008).

SUMO was used for the first time during the Flow over and around Hofsjökull (FLOHOF) field campaign (Reuder et al. 2012a) in central Iceland, 2007. Data from SUMO have subsequently been used to validate WRF boundary layer schemes for case studies from FLOHOF (Mayer et al. 2010).

The SUMO measurements have been verified against and shown to have a quality similar to that of well established sounding systems like radiosondes (Mayer et al. 2012; Jonassen 2008) and the authors are therefore confident in using these data for assimilation and model validation.

During take-off and landing, the SUMO is operated manually and wind data from the lowest tens of meters above the ground level are therefore not included in the data assimilation. Each of the profiles is averaged in 20-m height intervals. The descent data are used for the assimilation since these are found to have the better quality as the descent rate is slightly lower than the ascent rate. The lower descent rate gives the temperature and humidity sensor better time to adjust to its ambient surroundings, thus reducing the effect of slow sensor response, while also allowing for a more accurate determination of the wind vector.

An overview over the SUMO flights on 19 and 20 July is given in Table 1.

TABLE 1. SUMO flights made on 19 and 20 Jul 2009 during the Moso field campaign. The time is the average time during the flight descent. The lowest altitude with temperature and humidity observations is 10 m and for wind it is 70 m.

ID	Time (UTC)	Max altitude (m AGL)	Duration (min)
		19 Jul	
1	1238	3001	18
2	1300	1236	8
3	1319	1082	10
4	1339	1097	8
5	1358	1124	8
6	1518	1098	7
7	1541	1480	8
8	1605	953	7
9	1633	2830	14
10	1651	1204	9
11	1708	1437	13
12	1744	1200	10
13	1755	725	5
14	1822	1443	10
15	1841	1452	12
16	1856	1144	8
17	1914	1820	13
		20 Jul	
1	1109	2991	14
2	1157	1497	7
3	1306	1578	10
4	1410	1980	15
5	1507	1804	11
6	1607	2144	14
7	1710	1422	8
8	1809	1966	9
9	1832	1993	14
10	1932	607	8
11	2025	806	4

3. The numerical simulations

The numerical simulations are performed using the Advanced Research Weather Research and Forecasting Model (WRF-ARW) version 3.2.1 (Skamarock et al. 2008). The modeling system is fully compressible and is in this study run in nonhydrostatic mode using 3 two-way nested domains with a horizontal resolution of 9, 3, and 1 km. The outermost domain (855×810 km^2) covers Iceland and the surrounding waters (50–100 km offshore) while the innermost domain (250×190 km^2) covers southwest Iceland. In total, 51 vertical terrain-following model levels are used with an increased resolution toward the ground. The lowest half level is at approximately 9 AGL.

Two sets of 24-h simulations are performed: the first starting at 0000 UTC 19 July and the second at 0000 UTC 20 July 2009. The first 6 h of each simulation are considered as spinup. The Rapid Radiative Transfer Model (RRTM; Mlawer et al. 1997) scheme is used for longwave radiation parameterization, the Dudhia scheme

(Dudhia 1989) is used for shortwave radiation, and the Unified National Centers for Environmental Prediction–National Center for Atmospheric Research (NCEP–NCAR)–Air Force Weather Agency (AFWA) Noah land surface model (Chen and Dudhia 2001) is used with soil temperature and moisture in four layers for surface physics. Furthermore, the Yonsei University Scheme (Hong et al. 2006), a nonlocal-k theory, first-order scheme with an explicit entrainment layer, is used for the parameterization of boundary layer physics.

Operational analysis from the ECMWF at 91 model levels and 0.125° horizontal resolution is used to initialize and force the model at its boundaries every 6 h.

The extent of the ever-retreating edges of the ice caps in Iceland is too large in the standard 24-category U.S. Geological Survey (USGS) land-use dataset compared to reality. An updated version of the 24-category USGS land-use dataset with more realistic ice cap extents provided by the Institute for Meteorological Research (Reiknistofa í Veðurfræði/Belgingur) is therefore used in the simulations of this study (Rögnvaldsson et al. 2007).

Four-dimensional data assimilation (FDDA)

The FDDA technique has been described and employed in several studies (e.g., Anthes 1974; Stauffer and Seaman 1990, 1994; Schroeder et al. 2006). Various datasets from a range of atmospheric measurement platforms have been assimilated using FDDA, both for local and regional hindcasting, nowcasting, and forecasting applications. However, to the knowledge of the authors, data from UASs have never before been used for these purposes.

There are two main types of nudging available in the WRF FDDA system (Liu et al. 2005). One is the analysis nudging where the model state is nudged toward a gridded analysis field, which is often used at larger scales for coarse grid resolutions. The second is the observation nudging, which is used in this study. In observation nudging, each observation is used to nudge the model within a certain horizontal radius surrounding its location and within a given time window. The nudging is controlled by the nudging term, being proportional to the difference between the observed and simulated atmospheric state. The nudging is reduced as the distance in time and space from the observation to the model grid point increases. The parameters being nudged are the horizontal wind components u and v, the specific humidity, and the temperature.

The nudging's influence in time is limited to 40 min before and after each observation, with the strength of the nudging being ramped down toward the beginning and end of each time interval.

TABLE 2. WRF FDDA sensitivity experiments with different radii of influence R and nudging coefficients G.

Name	R (km)	G (s^{-1})
FDDA R1G1	100	6×10^{-4}
FDDA R2G1	50	6×10^{-4}
FDDA R3G1	150	6×10^{-4}
FDDA R1G2	100	3×10^{-4}
FDDA R1G3	100	12×10^{-4}

The strength of the nudging is controlled through the nudging coefficients G. The horizontal radius of influence R determines the size of the area that is directly affected by the nudging. Studies have shown that the values of G and R can be important for the data assimilation results (e.g., Xu et al. 2002). In this study, several FDDA sensitivity experiments are carried out and validated against AWS observations with the aim to find the optimal combination of these two parameters. The values tested for G are the default 6×10^{-4} s^{-1} in addition to 3×10^{-4} s^{-1} and 12×10^{-4} s^{-1}. The parameter R is given the value 100 km, which covers approximately the innermost domain, and thus the area of main interest, as well as 50 and 150 km. In each of the simulations, the same values for G and R are used for all the nudged parameters and nested domains. In these experiments, all 17 UAS soundings from case 1 (19 July) and all 11 UAS soundings from case 2 (20 July) are used for assimilation. Both the mass fields (temperature and humidity) and the horizontal wind fields are assimilated.

Table 2 gives an overview over the values of R and G used for the corresponding FDDA sensitivity experiments.

A third factor, that influences the nudging, is the weighting function used to apply the nudging. Changing this is not as straightforward as changing the R and G parameters and is therefore left to a future study.

The results from the FDDA sensitivity experiments with different values of R and G are presented in the first part of the results section in this article. The best combination of R and G is defined as the one giving the best validation against AWS data. In the second part of the results section, a CTRL setup using no data assimilation is compared against four different FDDA setups using the best combination of R and G. In the FDDA-all setup, all UAS soundings are assimilated. In the FDDA-nomass and FDDA-nowind setups, the mass fields and wind fields, respectively, are left out of the assimilation. These latter experiments are performed to evaluate the relative importance of assimilating the wind and mass parameters for the case studies. In the FDDA-single setup, both the mass and the wind fields are assimilated, but only the first sounding in each case is used. This latter experiment is included to evaluate how long lasting the impact of assimilating a single profile is and can be considered a dynamical initialization.

No observations from the AWSs are used for assimilation in any of the FDDA simulations.

4. Results

a. The near-surface flow

During 19 and 20 July 2009, Iceland was under the influence of a northeasterly synoptic flow, set up by a low pressure system over the British isles to the southeast of Iceland and a high pressure ridge over Greenland to the northwest (Fig. 2). At the observation site of Eyrarbakki, the skies were dominated by a layer of stratocumulus clouds that increased in thickness and horizontal extension during the course of both these days.

Figure 3 gives a more detailed overview of the flow over Iceland. The simulated flow compares reasonably well against AWS observations spread throughout
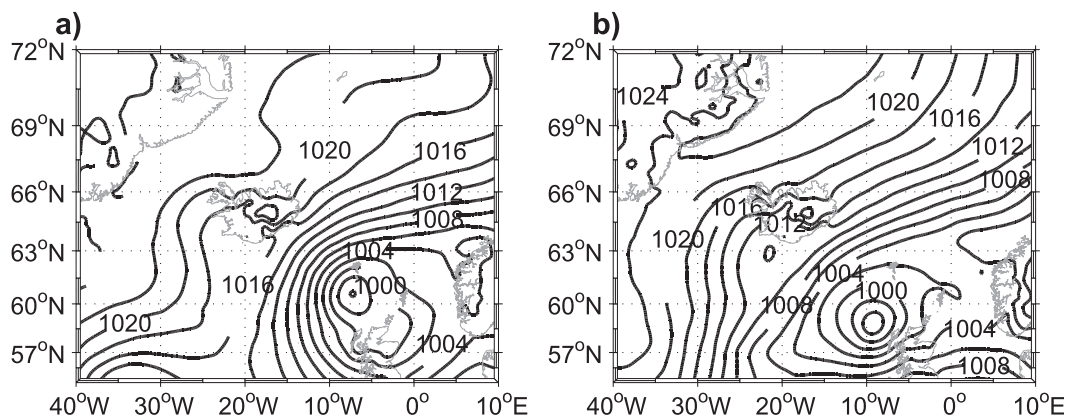

FIG. 2. Mean sea level pressure (hPa) at 1200 UTC (a) 19 Jul and (b) 20 Jul 2009, based on analysis from ECMWF.
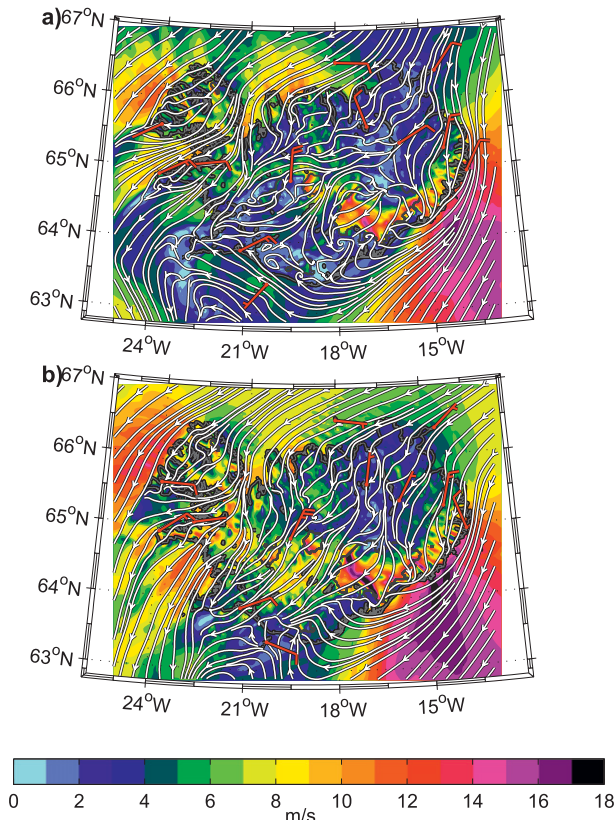
FIG. 3. Simulated near-surface (10 m) winds from the CTRL simulations at 1200 UTC (a) 19 Jul and (b) 20 Jul 2009 for domain 2 (3-km horizontal resolution). Surface observations from AWSs are indicated with red wind barbs. Each half barb represents 2.5 m s^{-1}.

Iceland and it can be seen that the general flow in case 2 (20 July) is somewhat stronger than in case 1 (19 July).

b. Determining the optimal combination of the radius of influence R and the nudging coefficient G

As outlined in section 3, an effort is made to determine the best combination of the R and G parameters in the FDDA setup. Figure 4 shows root-mean-square and mean errors (RMSE and bias) between the available AWS data and the CTRL and FDDA experiments using different values of R and G. A clear trend toward an improvement in both the temperature and wind is seen for both case 1 and case 2 when comparing the error statistics of the CTRL experiment to the FDDA experiments. For the temperature in case 1, the RMSE lies in the range 1.5–1.7 K for the FDDA simulations and it has a value of 2.1 K for the CTRL simulation. For case 2, the temperature RMSE is 1.6 K for all the FDDA simulations and 1.9 K for the CTRL simulation.

For the wind speed and wind direction error statistics, the vector wind difference (VWD) is used. VWD is defined as follows:

$$VWD = [(u_o - u)^2 + (v_o - v)^2]^{1/2}, \qquad (1)$$

where (u_o, v_o) and (u, v) are the observed and simulated horizontal wind components, respectively. The RMSE of the VWD is in case 1 reduced from 3.7 m s^{-1} in the CTRL simulation to 3.3–3.4 m s^{-1} in the FDDA simulations. Similarly, the RMSE of the VWD is reduced from 5.0 m s^{-1} to 4.6–4.7 m s^{-1} in case 2.

The statistics for the specific humidity, on the other hand, give more variable results with no such consistent improvement.

Overall, there are only marginal differences in the error statistics between the different FDDA experiments and an investigation of the horizontal fields of temperature, humidity, and wind confirms this impression (not shown). The default G of 6×10^{-4} s^{-1} and a moderate R of 100 km are therefore used in the rest of this study. The R of 100 km covers approximately domain 3, which is the area of interest in this study.

c. General results

In both the studied cases, sea-breeze circulation dominated the atmospheric flow characteristics and surface fields of temperature and humidity. Thus, in the following evaluation of the numerical simulations, special attention is paid to how the model manages to capture the sea breezes' onset, maximum horizontal extension, and final decay with and without the UAS data assimilated. The model results are verified against available AWS data using the sea-breeze front as the main diagnostic. The inland progression of the sea breeze is marked by its front, which might be viewed as a mesoscale cold front. The passage of this front typically encompasses a drop in surface temperature in the order of several kelvins, an increase in humidity, and a turn in wind direction.

Figures 5, 6, and 7 show the simulated and observed wind speed and wind direction, temperature, and specific humidity at selected AWSs in southwest Iceland on 19 (case 1) and 20 July (case 2) 2009.

In the following, the results from each of the two cases are described separately. Case 2 is described in less detail than case 1 and a main emphasis in the description of case 2 is put on where the results from the two cases differ the most.

1) CASE 1: 19 JULY

On 19 July, the first signs of sea breeze are seen at Hella, Iceland. The onset of the sea breeze, which takes place at 1000 UTC, can be detected by an abrupt halt in the increase of temperature (Fig. 6). This is associated
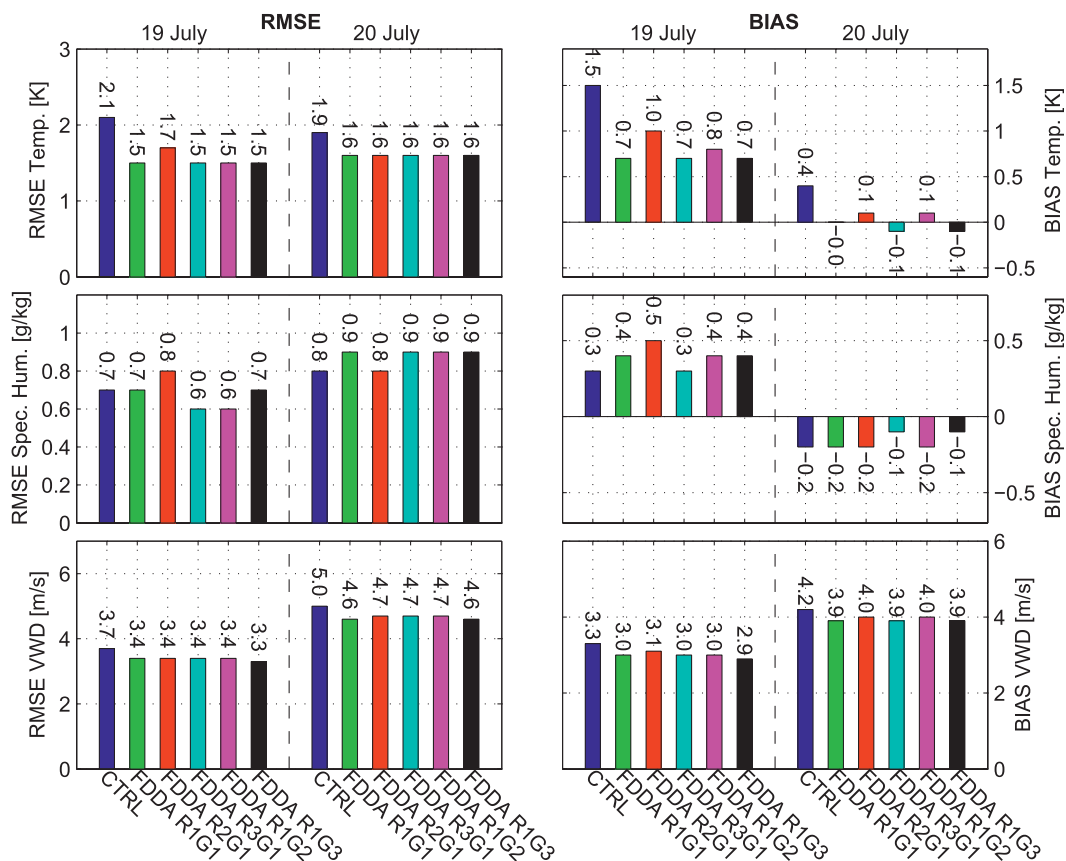
FIG. 4. Error statistics for the CTRL and the FDDA experiments using different combinations of the radius of influence R and nudging coefficients G. Table 2 lists and explains the different experiments.

with the winds turning to the southeast (Fig. 5). The halt in the temperature increase is captured by the model, but it takes place 2–3 h earlier. The onshore flow at Hella is visible in the 1200 UTC near-surface wind field (Fig. 3). The largest difference between the WRF simulation using only one UAS profile (FDDA-single) and the simulation using all 17 profiles (FDDA-all) at Hella is found in the temperature from 1800 to around 2100 UTC. Between those hours, the temperature is underestimated by 2–3 K in the FDDA-single simulation and lies within 1 K in the FDDA-all simulation. The temperature at Hella in the simulation using all UAS profiles, but no wind information (FDDA-all-nowind) lies much closer to the FDDA-all than does the FDDA-all-nomass at Hella throughout the simulation.

The sea breeze is stronger and penetrates farther inland in the FDDA-all simulation than in the CTRL simulation (Fig. 8). There is also a local enhancement of the synoptic-scale flow, opposing the sea breeze in the FDDA-all simulation.

The observed maximum inland penetration of the sea breeze on 19 July takes place around 1600 UTC. It then touches upon Kalfholl, Iceland, as marked by an observed intermittent shift from northerly to southerly flow and a short-lived increase in humidity at this station. The increased humidity follows closely the observed increase in the FDDA simulations, except in the FDDA-all-nomass simulation, which, similar to CTRL, lacks such an increase. Thus, the horizontal extension of the sea breeze is longer in the FDDA simulations (except FDDA-all-nomass) than in the CTRL simulaton, and the validity of the longer inland sea-breeze penetration is confirmed by observations, at least for the area represented by Kalfholl.

As for virtually all AWSs, there is a nearly consistent temperature underestimation in the CTRL simulation at Kalfholl, but at this station, it is still significant (3–4 K in case 1) even after assimilating all UAS profiles using both the mass and wind fields.

At Eyrarbakki, the UAS operation site, the sea breeze starts between 1200 and 1300 UTC, which is marked by a drop in the observed temperature and a shift from northeasterly to southwesterly winds. The FDDA-all simulation corrects for a temperature underestimation
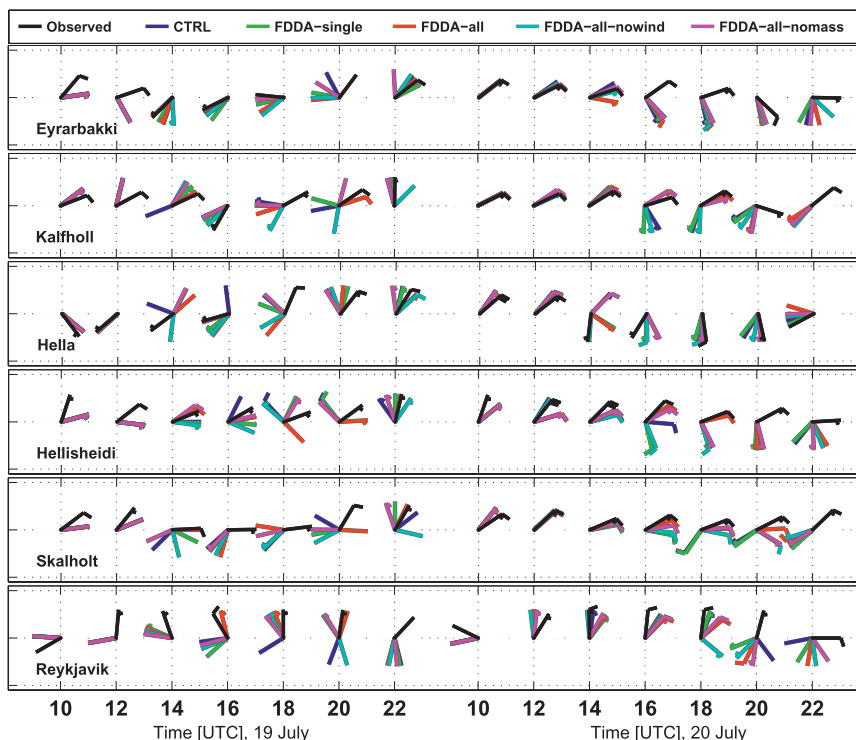
FIG. 5. Observed and simulated 10-m wind direction (°) and wind speed (m s^{-1}) at selected surface stations on 19 and 20 Jul 2009. Each half barb represents 2.5 m s^{-1}. The simulation results are from domain 3 (1-km horizontal resolution).

that is seen in the CTRL simulation at Eyrarbakki from 1200 until around 2000 UTC, when the bias in the CTRL simulation reaches 2–3 K. The FDDA-single simulation temperature gradually degrades from a near perfect match with the observation at Eyrarbakki at 1200 UTC to a similar value as in the CTRL simulation at around 1900 UTC.

At Hellisheidi, Iceland, there are no observed signs of sea breeze at any time of the day. This absence of sea breeze is most likely due to the station's elevated location (360 MSL). With the exception of the morning hours (before 1200 UTC), 1700 UTC, and toward midnight, the temperature is underestimated by some 2–3 K in the CTRL simulation. In the FDDA-all simulation, on the other hand, the temperature is reproduced very well with observation-model differences of the order of 0–1 K. In the FDDA-single simulation, the temperature bias lies somewhere between the CTRL and FDDA-all simulation (1–2 K) from 1200 UTC onward for most of the day. After 1700 UTC, the FDDA-all-nomass simulation performs better than the CTRL simulation with respect to 2-m temperature. The underestimated temperature in the CTRL simulation can at least in part be related to a shift from the observed northeasterly to northwesterly flow in the CTRL simulation between 1600 and 1800 UTC.

Farther inland, at Skalholt, Iceland (approximately 40 km from the coast), there are also no observed signs of sea breeze. Similar to Kalfholl, the temperature is significantly underestimated in all the simulations, but not as much in the FDDA-all-nowind as in the FDDA-all-nomass and CTRL simulations. As at Kalfholl, the improvement in the FDDA-single simulation temperature is relatively short lived and is gone after approximately 6 h.

The simulated wind speed at Skalholt is very low (less than 2.5 m s^{-1}) at 1600 UTC and it has a southerly component, coinciding with the sea-breeze direction. The simulated humidity, however, does not show any increase for any of the simulations at this location (not shown), which would have been expected if the sea breeze had reached it.

The largest changes in temperature from the CTRL to the FDDA simulations are found in area west, where the CTRL simulation temperatures are largely underestimated in the area around Reykjavik and over parts of the Reykjanes peninsula. This bias is connected to two interdependent phenomena. A shallow (50–100 m) fog resides from early morning hours (0600 UTC) to late evening (2100 UTC) along the Reykjanes peninsula to the southwest of Reykjavik in the CTRL simulation
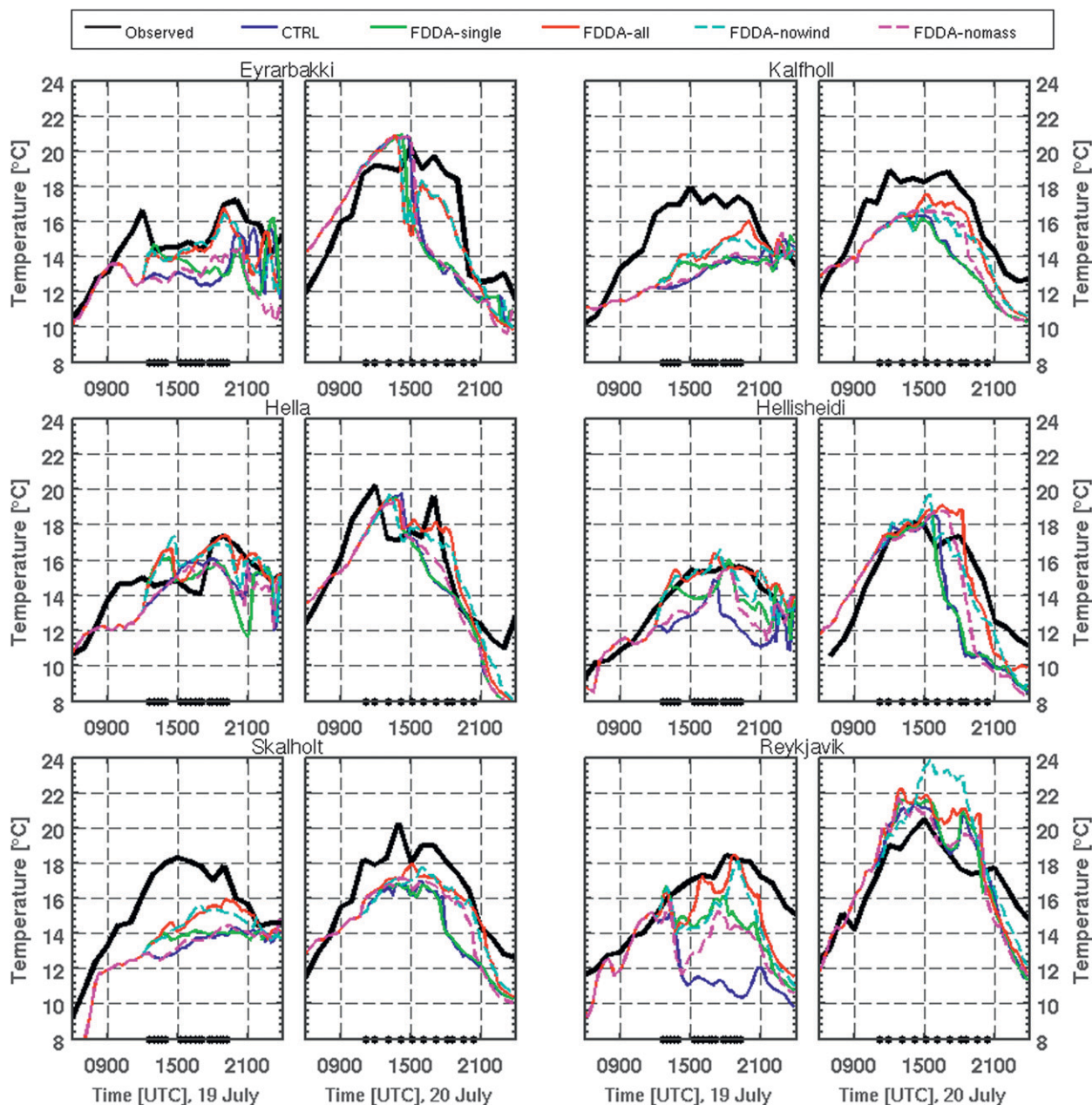
FIG. 6. Observed and simulated 2-m temperature (°C) at selected AWSs on 19 and 20 Jul 2009. The simulation results are from domain 3 (1-km horizontal resolution). Black dots at the bottom line of each *x* axis indicate the time of UAS soundings.

(e.g., Fig. 8). In the FDDA simulations, this fog disappears before 1400 UTC. In the CTRL simulation, there is an onshore flow from the aforementioned fog, advecting cold and moist air into the region. This is evident in the form of low temperatures and relatively high values of humidity at the stations in the area in the CTRL simulation (e.g., Reykjavik and Grindavik, Iceland, Fig. 7). In the observations and also mostly correctly in the FDDA simulations, the flow to the north and west of

Reykjavik is from the north (Fig. 8). Both the assimilation of only the UAS wind profiles (FDDA-all-nomass) and the assimilation of only the UAS temperature and humidity profiles (FDDA-all-nowind) aid in removing this fog, with the effect of the latter being larger.

2) CASE 2: 20 JULY

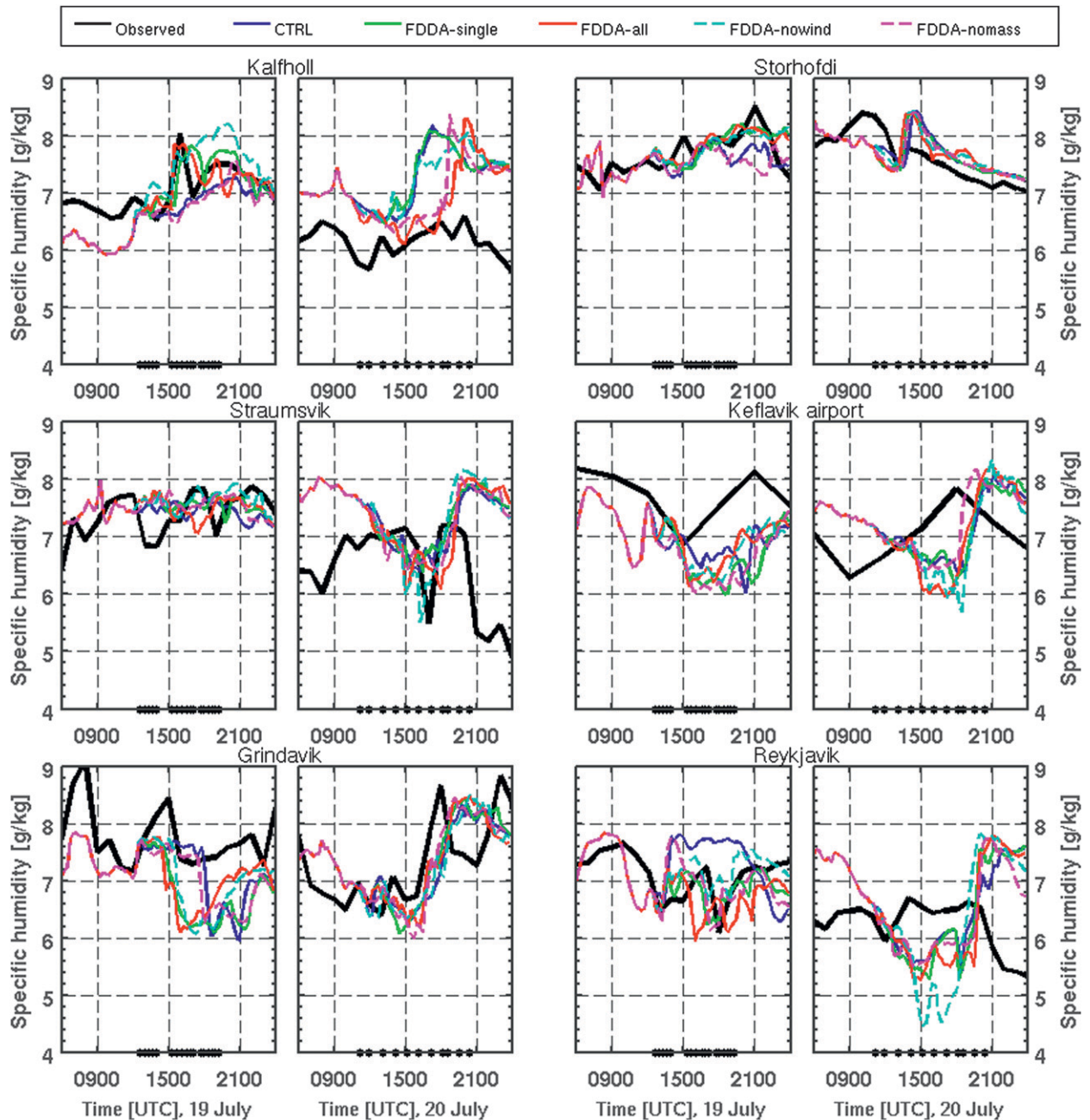On 20 July, the sea breeze sets on later than in case 1 and the first signs of a sea breeze are again found at

FIG. 7. Observed and simulated 2-m specific humidity (g kg^{-1}) at selected AWSs on 19 and 20 Jul 2009. The simulation results are from domain 3 (1-km horizontal resolution). Black dots at the bottom line of each x axis indicate the time of UAS soundings.

Hella, taking place between 1200 and 1300 UTC. Except for the CTRL and FDDA-all-nomass simulations, the model times the correspondent change to southerly wind quite accurately, while the drop in temperature lags some 1–2 h behind what is observed in all the simulations.

In contrast to case 1, the sea breeze in case 2 penetrates farther inland in the CTRL than in the FDDA-all simulation (Fig. 9). A sea breeze is never observed at

Kalfholl. In the CTRL, FDDA-all-nowind and FDDA-single simulations, however, there is an onset of sea breeze at Kalfholl at around 1600 UTC and it lasts until at least 2200 UTC. The remaining FDDA simulations correctly contain no sea breeze between 1600 and 1800 UTC at Kalfholl, but in these simulations the sea breeze erroneously reaches the station at around 2000 UTC. The presence of the sea breeze is evident by the increase in
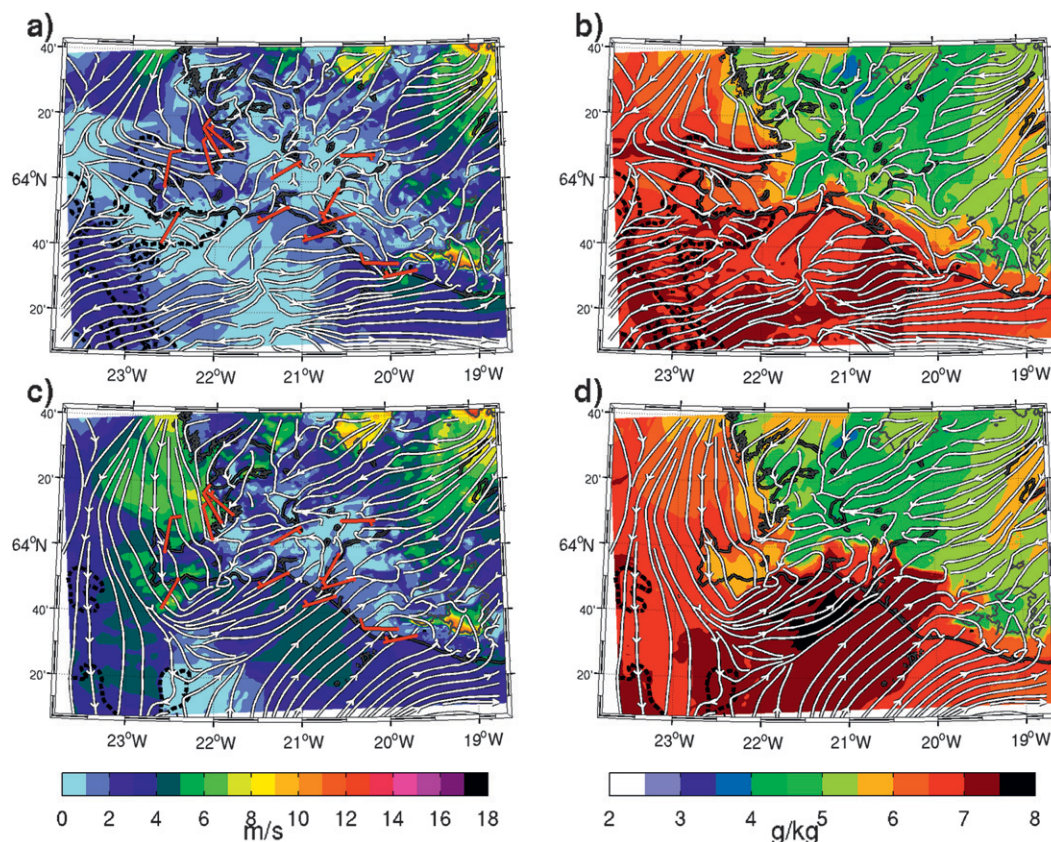
FIG. 8. Simulated 10-m wind speed (m s^{-1}) and wind direction and specific humidity (g kg^{-1}) from the lowermost model half level (approximately 9 m AGL) in domain 3 (1-km horizontal resolution) at 1600 UTC 19 Jul 2009 for the (a),(b) CTRL simulation and (c),(d) FDDA-all simulation. Observations of wind speed and wind direction at selected surface stations are included as well (red wind barbs). Each half barb represents 2.5 m s^{-1}. Areas with over 98% relative humidity are encircled by a black, dashed line.

humidity at Kalfoll at 1500–1600 UTC in CTRL, FDDA-all-nowind, and FDDA-single and 1900–2000 UTC in FDDA-all and FDDA-all-nomass, respectively.

At Eyrarbakki, the sea breeze is only observed for a short period of time around 2000 UTC. In all the simulations, on the other hand, there is an onset of sea breeze at Eyrarbakki at 1500 UTC. This is marked by a sharp drop in the simulated near-surface temperature in the CTRL, FDDA-all-nomass, and FDDA-single simulations, whereas in the FDDA-all and FDDA-all-nowind simulations, the temperature keeps closer to the observed one with a discrepancy of around 2 K.

The FDDA-all-nowind and FDDA-single simulations erroneously contain sea breeze at Hellisheidi between 1600 and 2200 UTC and so do the rest of the simulations between 2000 and 2200 UTC.

In contrast to the results of case 1, there is seemingly no, or only very little, improvement with respect to temperature in the FDDA-single simulation for any of the stations for case 2. While the simulated sea breeze did not

reach Skalholt in case 1, the CTRL and FDDA-single simulations of case 2 do contain sea breeze at Skalholt, setting on at 1800 UTC and lasting until at least 2200 UTC, which is identified in terms of both a southerly wind and a lowered temperature at this location. The remaining FDDA simulations improve on this situation and they do not contain sea breeze at Skalholt before 2200 UTC, at which they show an erroneous southerly wind direction. As in case 1, relatively large underestimations of temperature are found at Kalfholl and Skalholt.

3) ERROR STATISTICS

The RMSE and mean bias statistics of the simulated and observed near-surface temperature, specific humidity, and wind (Figs. 10 and 11), largely support the impression gained by the above subjective analysis of the WRF simulations against the AWS observations. A main effect of assimilating the UAS data is the reduction of a nearly consistent model temperature underestimation. The largest contribution in mitigating this bias comes
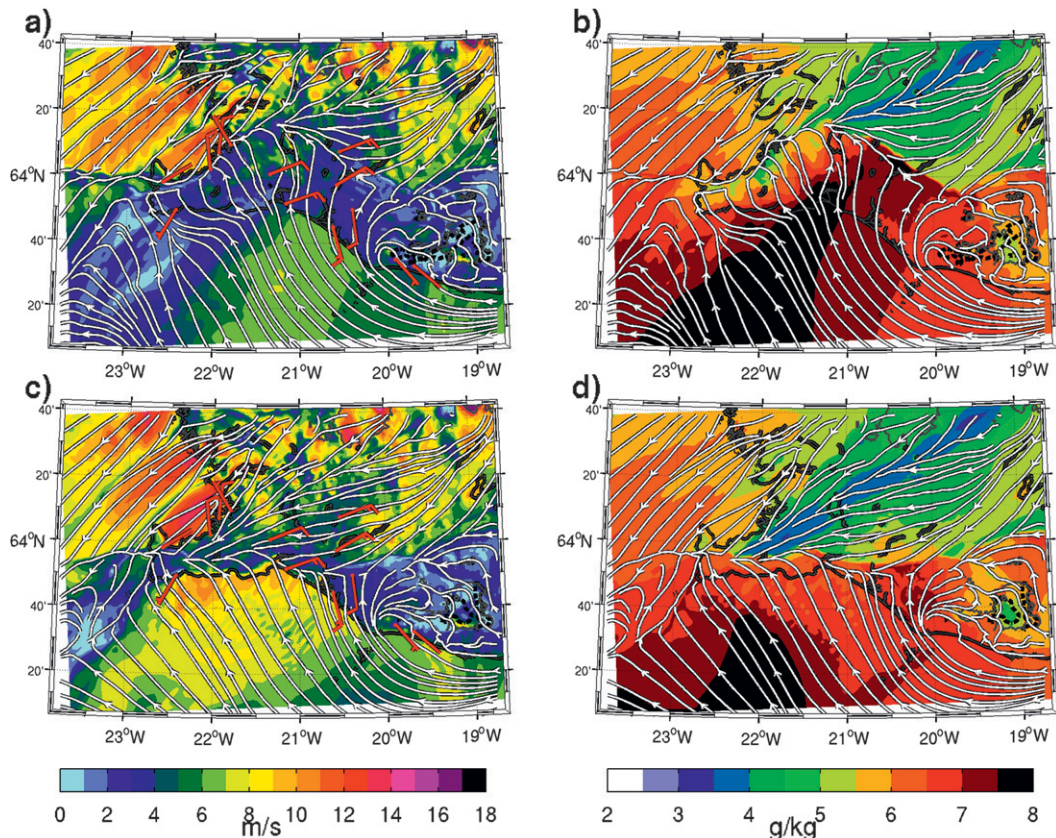
FIG. 9. As in Fig. 8, but for 1800 UTC 20 Jul 2009.

from the assimilation of the UAS temperature and humidity data. The error reduction is largest in the FDDA-all simulations, where the average RMSE between the modeled and observed (AWS) 2-m temperature in case 1 is reduced from 2.1 to 1.5 K and the corresponding averaged biases from 1.5 to 0.7 K. In case 2, the reduction is somewhat smaller, with the average RMSE being reduced from 1.9 to 1.6 K and average bias from 0.4 to 0 K.

The effect of only assimilating the wind data (FDDA-all-nomass) is least among the FDDA simulations in this regard, but still positive with an average RMSE of 1.9 K and average bias of 1.3 K for case 1 and an average RMSE of 1.8 K and average bias of 0.3 K for case 2.

In case 1, the RMSE reduction from the FDDA-single simulation lies between the CTRL and FDDA-all simulations with an average RMSE of 1.7 K and average bias of 1.1 K. It should, however, be noted that the observation-model difference for the FDDA-single simulation increases with time, as shown above, starting at differences similar to the FDDA-all simulation and slowly approaching the CTRL simulation in accuracy and the two are very similar after 6–7 h at most stations.

In case 2, there is no such consistent improvement in the FDDA-single simulation, and for some AWSs the error statistics is the same as or even worse than for the CTRL simulation. It can also be seen in the previously presented time series from the selected AWSs that the improvement is very short lived in case 2 when compared to case 1 in the FDDA-single simulations.

For specific humidity, there is no consistent improvement when using FDDA. Nevertheless, for individual stations like Reykjavik, there is still an improvement in case 1, which is caused by the false presence of fog along the nearby coast in the CTRL simulation, as commented on earlier.

The average of the RMSE VWD in case 1 is reduced from 3.7 m s^{-1} in the CTRL simulation to 3.4 m s^{-1} in the FDDA-all simulation. The main contribution comes from the assimilation of the wind as the average VWD RMSE assimilating only the wind is 3.5 m s^{-1}, whereas when assimilating only the mass parameters it is 3.6 m s^{-1}. The largest improvements in VWD among the stations when using FDDA in case 1 are found at the AWSs of Arnes and Mork. This improvement is caused by a more accurate description (higher wind speeds) of the local
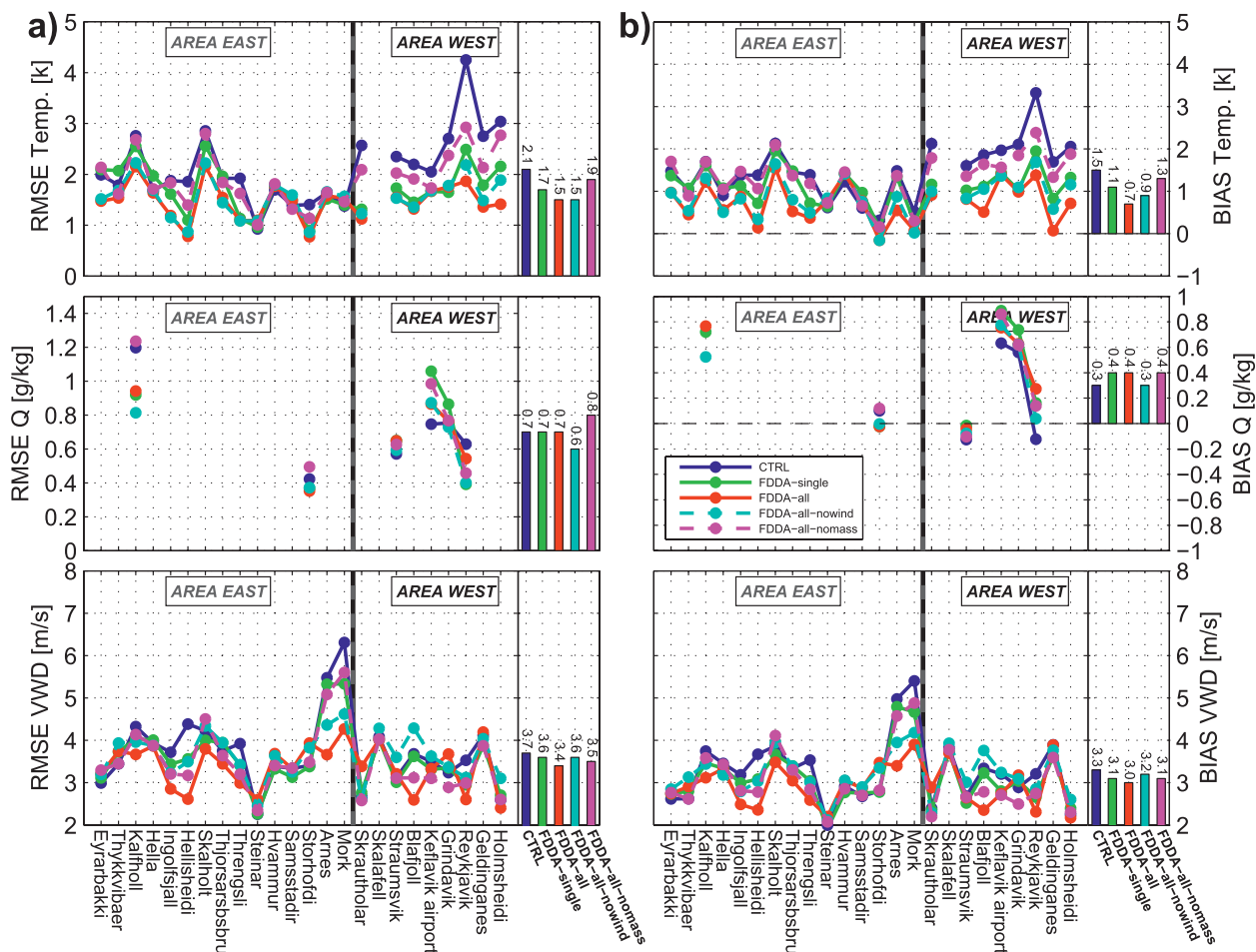
FIG. 10. (a) RMSE and (b) bias (mean error) between observed and simulated 2-m temperature, 2-m specific humidity, and 10-m vector wind difference (VWD) for 19 Jul 2009. Mean values of the RMSE and bias for all stations for each simulation are given with vertical bars. Area east is where the studied sea-breeze events took place.

component of the northeasterly synoptic flow, as evident in the horizontal 10-m wind field (Fig. 8). Also in case 2, there is an improvement in the VWD statistics when assimilating the UAS wind data. The average RMSE of the VWD is reduced from 5.0 (CTRL) to 4.6 m s^{-1} (FDDA-all).

d. The flow aloft

In the study of the flow aloft, we focus mainly on the location of Eyrarbakki, where the UAS soundings were made. A main emphasis is put on the description of the vertical development of the sea-breeze circulation and how this is captured by the model, with and without all and only parts of the UAS data assimilated. As for the surface flow, the flow aloft in case 1 and case 2 is described separately and a main emphasis in the description of case 2 is put on where the two cases differ the most.

1) CASE 1: 19 JULY

Figures 12 and 13 show time series of observed and simulated atmospheric profiles of temperature, specific humidity, wind speed, and wind direction on 19 and 20 July. The first UAS profile (1238 UTC 19 July) was measured just after the onset of the sea breeze at Eyrarbakki. The sea breeze is identifiable in the first four UAS profiles as a layer of low temperatures and relatively high humidity below approximately 250 AGL. In this shallow layer, winds are from the sea contrasting the northeasterly synoptic flow further aloft. Approximately at the top of this layer, the on- and offshore flows meet and there is a distinct wind speed minimum. Using the criteria of low wind speed, a turn in wind direction, an increase in temperature and decrease in humidity, the highest vertical extension of the sea breeze of 250–300 AGL is reached sometime between 1400 and 1600 UTC. At 1900 UTC, there are no longer
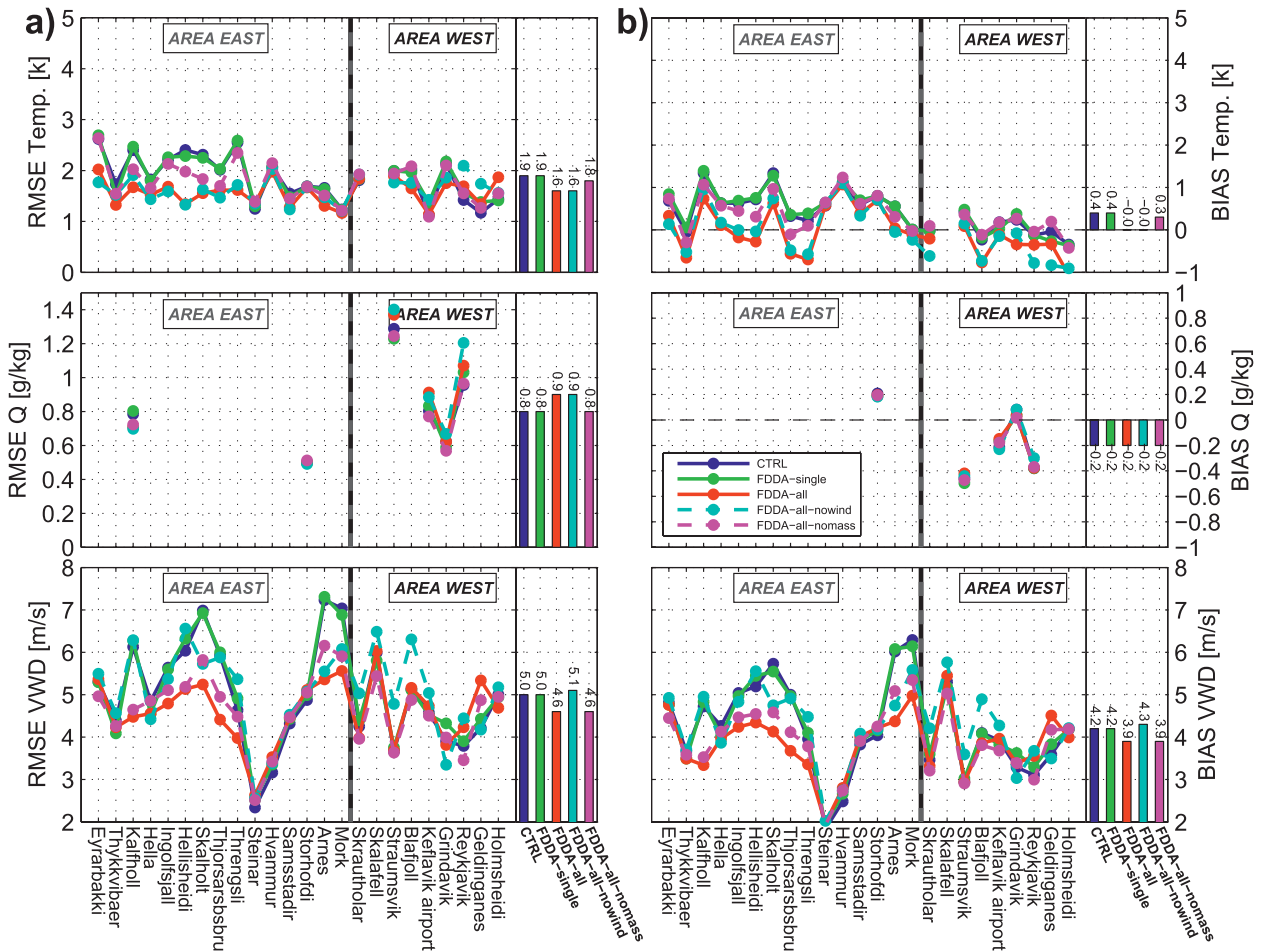
FIG. 11. As in Fig. 10, but for 20 Jul 2009.

any signs of sea breeze in either the UAS profiles or in the AWS observations.

The simulated temperature, humidity, and wind profiles in the FDDA-all simulations are, not surprisingly, considerably closer to the observed data from the UAS and should not be used for direct comparison with the other simulations. The FDDA-single profiles are not discernable from the FDDA-all profiles at 1238 UTC.

The temperatures in what may be interpreted as the boundary layer (below an inversion at 1–1.2 km) are underestimated in the CTRL simulation by 2–3 K compared to the three first UAS profiles (1238, 1358, and 1604 UTC). The specific humidity, however, is well reproduced by the model in these first three profiles, while there are larger discrepancies in the two last profiles (1743 and 1914 UTC).

The temperature underestimations of the lower troposphere are similar in magnitude to the average underestimation in the simulations of temperature at the AWSs. These temperature and humidity differences are reflected in the RMSE and BIAS values averaged over all profiles throughout the day (Fig. 14).

The sea-breeze layer is not evident in the two first profiles (1238 and 1358 UTC) of temperature and humidity in the CTRL run, whereas it is present in the observations. The wind direction, however, shows southerly flow below 500 AGL in these profiles. Judging by the wind direction, this indicates an approximately 250 m deeper sea breeze in the CTRL simulation than in the observations and FDDA simulation. The simulated wind speed between 250 and 500 AGL is, however, very weak (below 2 m s^{-1}).

Toward the evening on 19 July (1744 and 1915 UTC profiles), the sea breeze is still evident in the CTRL simulation in temperature, humidity, and in wind direction. The CTRL simulation profiles of temperature above 250 AGL agree well with the observed and FDDA-simulated profiles for these two latter instances. Below, however, there is a temperature deficit of 2–3 K, indicating that the sea breeze is still present at Eyrarbakki in the
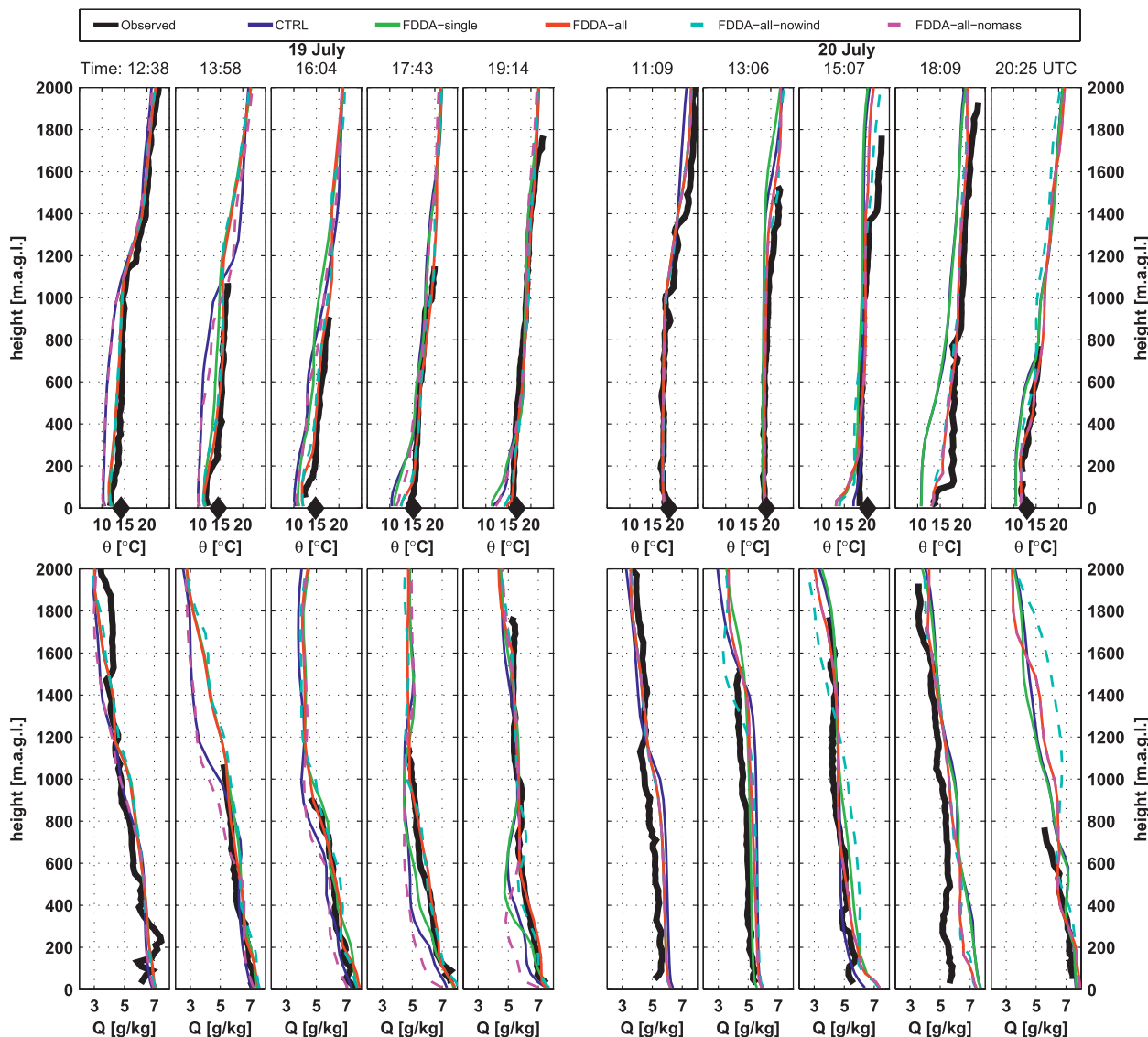
FIG. 12. Observed and simulated profiles of potential temperature θ and specific humidity Q from Eyrarbakki on 19 and 20 Jul 2009. Observations made by the AWS at Eyrarbakki are indicated with black diamonds. The 1809 UTC profile on 20 July is measured some 18 km to the east of Eyrarbakki.

CTRL simulation, while it is almost gone in the FDDA-all and FDDA-all-nowind simulations. At 1914 UTC, the sea breeze is gone in the observations, still somewhat present in the lowermost atmospheric layer in FDDA-all simulation and evident in the CTRL simulation.

Figure 15 shows a vertical cross section of wind speed, wind direction, and specific humidity at 1600 UTC.

The moist, southerly sea-breeze layer penetrates about 40 km inland in the FDDA-all simulation, which is 20–30 km farther than in the CTRL simulation along this cross section. In the FDDA-all simulation, the sea-breeze layer over the sea contains stronger winds than in the CTRL simulation.

2) CASE 2: 20 JULY

On 20 July, clear signs of sea breeze in the displayed profiles are only found at 1809 and 2025 UTC (Figs. 12 and 13). The former and its subsequent profile (1932 UTC, not shown) were measured some 18 km to the east of Eyrarbakki and the sea breeze set on slightly earlier at this location than at Eyrarbakki. At 1809 UTC, the sea breeze is clearly evident, but it is less than 200 m deep at this time. At 2025 UTC, there is sea breeze at Eyrarbakki and it reaches around 500 AGL.

The temperature of the lower troposphere is generally better reproduced by the model for the shown profiles
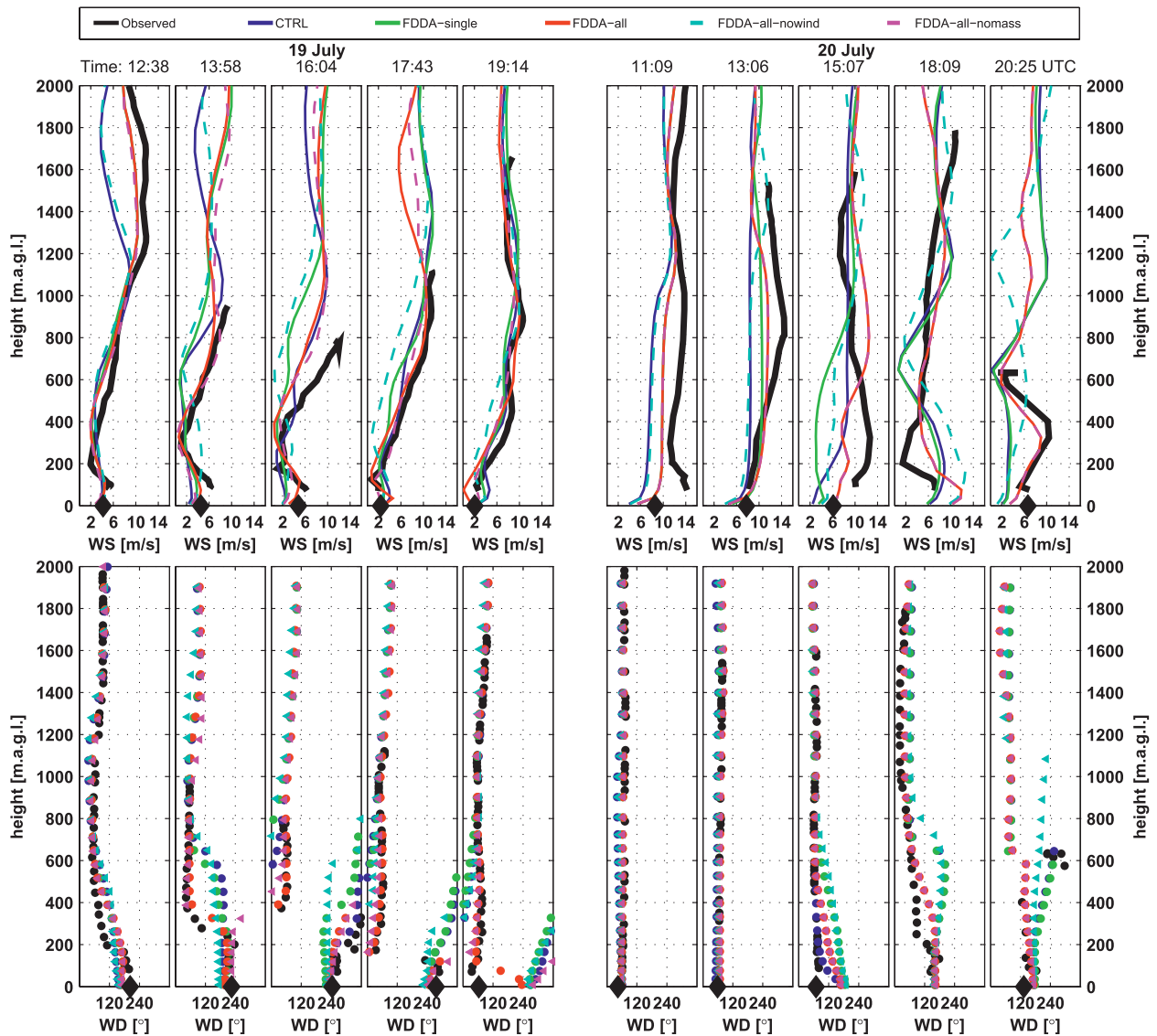
FIG. 13. As in Fig. 12, but for wind speed and wind direction.

than in case 1 and only in the 1809 and 2025 UTC profiles and the lower part of the 1507 UTC profile there are underestimations larger than 3 K.

As for the surface data, the approximation toward the CTRL values in the FDDA-single experiments happens considerably faster in case 2 than in case 1.

While the average temperature underestimations are about the same aloft as at the AWSs in case 1, they are slightly larger aloft than at the AWSs in case 2.

As seen in the horizontal wind and humidity fields (Fig. 9), the sea breeze penetrates shorter inland in the FDDA-all than in the CTRL simulation. Along the investigated cross section (Fig. 16), this difference amounts to around 40 km. The sea-breeze layer is also generally

shallower in the FDDA-all simulation. The offshore wind speed, however, is markedly stronger (more than 10 m s^{-1}) in the FDDA-all than in the CTRL simulation.

5. Discussion

In this study, it has been shown how profile data from a small UAS can be used for assimilation through the FDDA technique to improve high-resolution numerical simulations. The method has been applied to two summertime fair-weather situations that took place in southwest Iceland during the Moso field campaign on 19 and 20 July 2009.
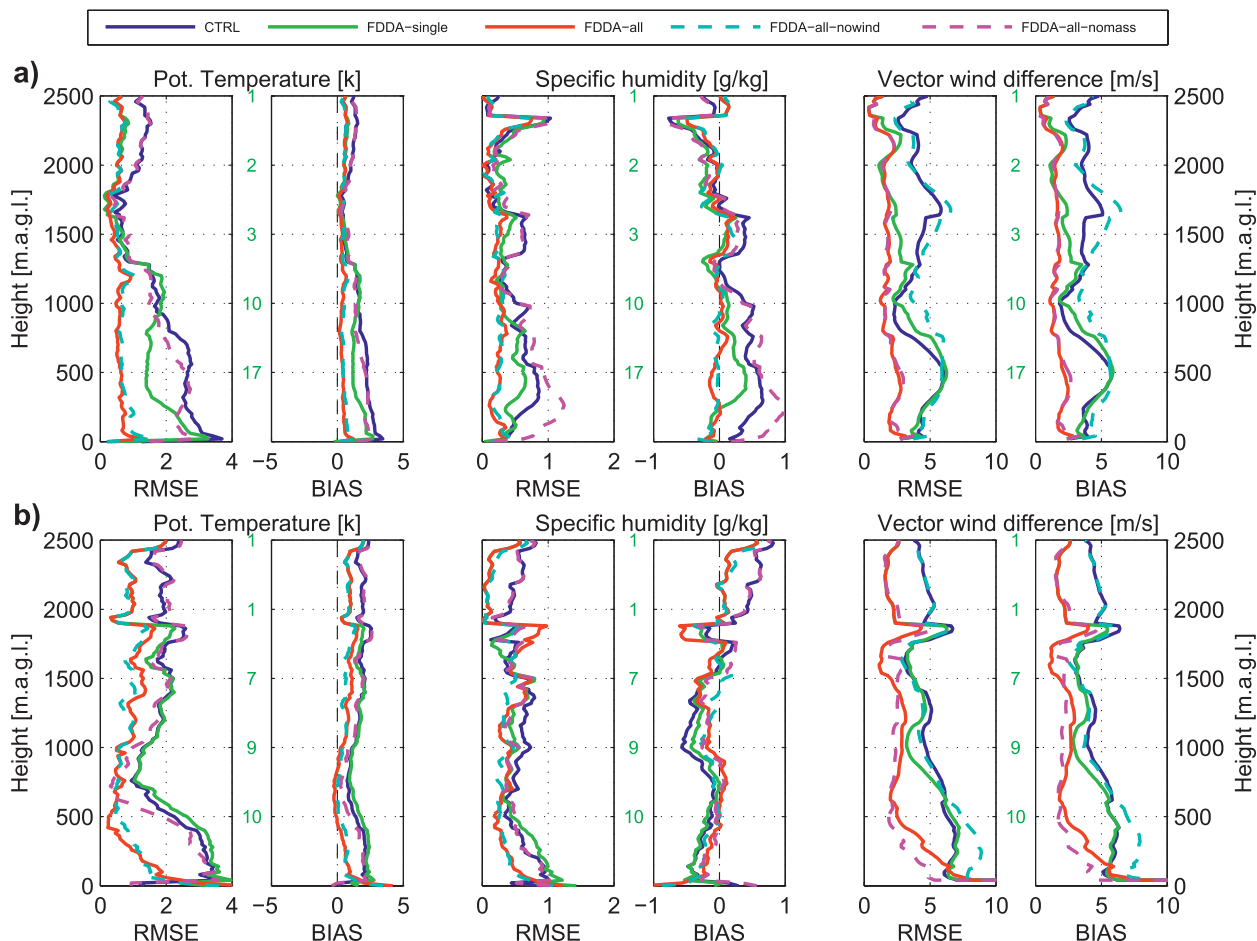
FIG. 14. RMSE and bias (mean error) between the observed and simulated atmospheric profiles of potential temperature, specific humidity, and vector wind difference at Eyrarbakki on (a) 19 Jul and (b) 20 Jul 2009. The numbers in green indicate the number of soundings reaching each respective height above the ground level.

The simulated near-surface flow compares generally well against observations from a relatively dense network of AWSs. Aloft, however, with exception to the 1200 UTC Keflavik radiosoundings, which compare well with the model (not shown), only the soundings made with the UAS were available for validation. It is therefore hard to estimate the validity of the impact of the assimilation on the flow field aloft. Similar future studies can definitely benefit from more soundings of this kind, both for validation and also for assimilation.

Previous studies (e.g., Xu et al. 2002) have shown that the choice of nudging coefficients and radius of influence can have an important effect on the FDDA data assimilation result. Thus, as a first step in this study, several FDDA sensitivity experiments were carried out using different combinations of the two parameters. The results reveal only a marginal sensitivity to the choice of these parameters for our case studies and for any of the tested combinations of the parameters the results are

markedly better than when using no FDDA at all. The default nudging coefficient of 6×10^{-4} s^{-1} and a radius of influence of 100 km, covering the area of interest, were therefore used for the rest of the study. These results are likely case dependent and more experiments with differing radii of influence for different domains and differing nudging coefficients for different parameters could prove beneficial, but are left for a future study.

The impact of the data assimilation on the model's representation of the sea-breeze circulation, which dominated the weather of southwestern Iceland during both studied situations, is large and positive, but it differs between the two investigated cases. In case 1, the assimilation leads to a sea breeze that penetrates farther inland and the sea breeze also has a sharper front. Away from the coast, farther inland, the assimilation of the UAS data gives a local enhancement of the synoptic-scale flow, opposing the sea breeze. The correctness of
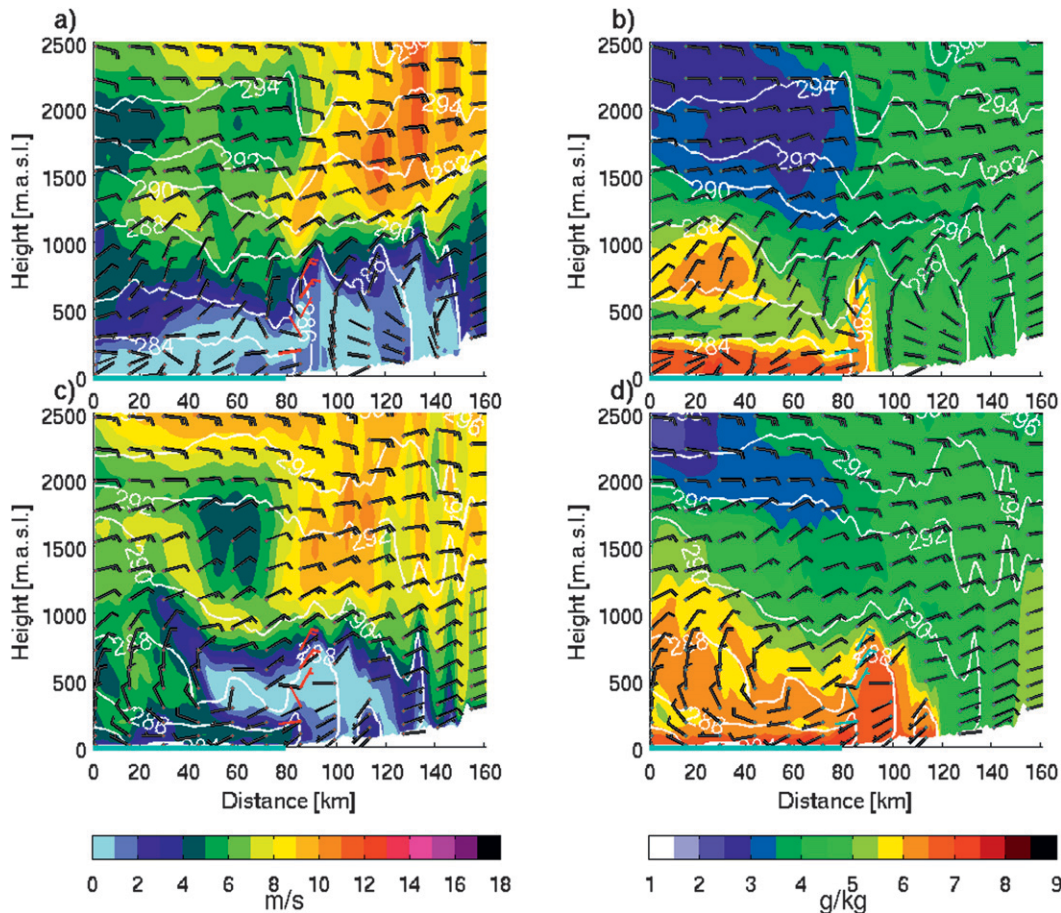
FIG. 15. Vertical cross sections of simulated wind speed and specific humidity at 1600 UTC 19 Jul 2009 for the (a),(b) CTRL simulation and (c),(d) FDDA-all simulation in domain 3 (1-km horizontal resolution). Isentropes are given with white contours at an interval of 2 K. Each half barb represents 2.5 m s^{-1}. The geographical location of the cross section is shown in Fig. 1. UAS wind measurements are indicated as well (red and cyan wind barbs). The offshore part is marked with a horizontal, solid line in cyan.

this latter flow enhancement is confirmed by two AWSs (Arnes and Mork) in the area. The sharpening of the sea-breeze front associated with increased speed of the sea breeze and stronger opposing winds is consistent with the findings of Gahmberg et al. (2010) on sea breeze and its relationships to synoptic flow. In case 2, on the other hand, the assimilation of the UAS data leads to a sea breeze that is weaker and that penetrates shorter inland.

Interestingly, the improvement seen when only assimilating the first profiles in each case (FDDA-single) is significantly larger and more long lasting in case 1 than in case 2. A possible explanation for this might be found in the differing synoptic conditions. Both cases had a northeasterly large-scale flow, but in case 2 it was stronger, which could potentially eradicate the impact of the assimilation faster than what is the case with the weaker flow in case 1.

A detailed physical interpretation of the FDDA simulation results is made difficult by the fact that the FDDA technique is based on terms in the prognostic model equations that are strictly speaking nonphysical. However, the impacts of the nudging coefficients are related to time scales of true physical processes and they should ideally be determined based on location and flow-dependent investigations. Nevertheless, the locally enhanced flow to the north of the investigated area in case 1 can be mainly attributed to a modification of the southwest Iceland thermal low, which is induced by higher boundary layer temperatures through the data assimilation. No such increase in wind speeds is seen when the UAS temperature data are left out of the assimilation.

Vastly underestimated surface temperatures are found in the vicinity of Reykjavik (e.g., up to 8 K in Reykjavik) in the simulation of case 1 without data assimilation. This
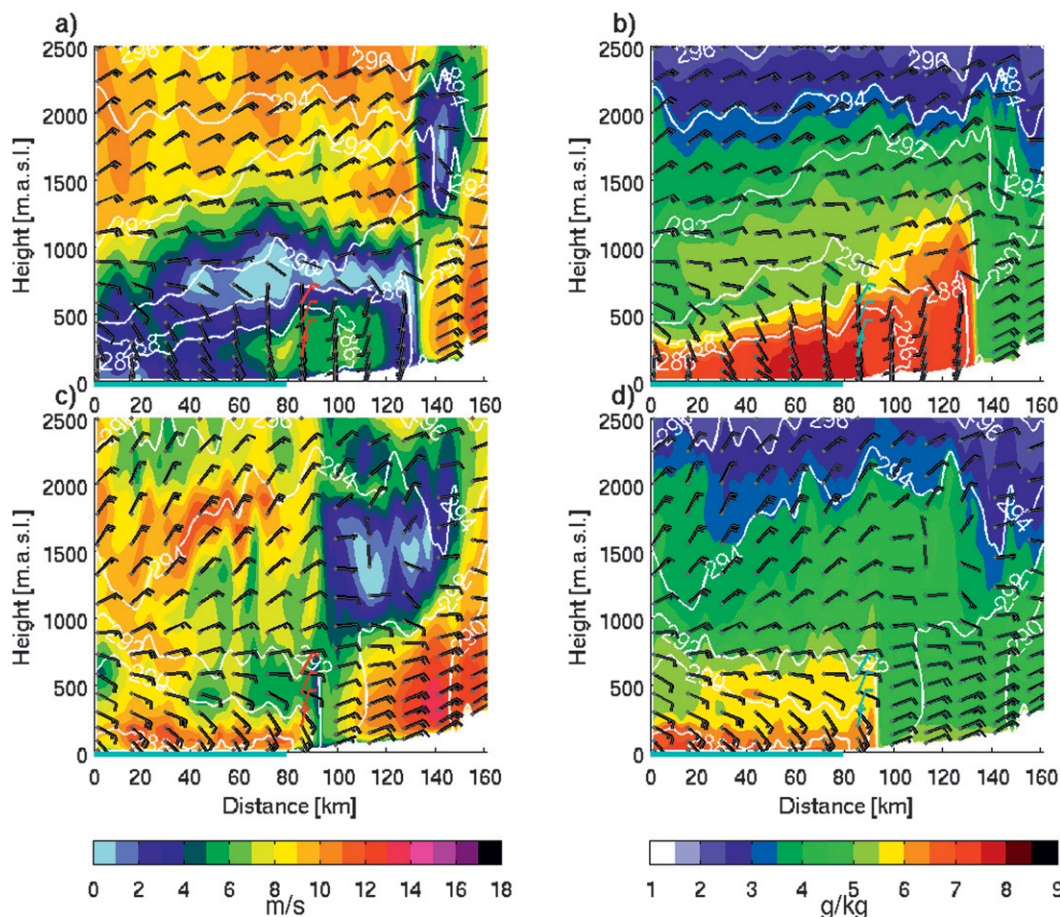
FIG. 16. As in Fig. 15, but for 1800 UTC 20 Jul 2009.

underestimation is caused by a fog that resides in the area for most of 19 July (see Figs. 7 and 8). All FDDA-simulations aid in removing this erroneous fog, with the effect of assimilating the mass data being the largest. The fog may be removed through at least two processes: the higher boundary layer temperatures induced by assimilating the UAS temperature data may evaporate the fog and the enhanced northerly flow to the north of Reykjavik (due to lower surface pressure over southwest Iceland) may transport the fog away. This northerly flow is also warmer than the air it replaces.

In both case studies, particularly large underestimations of the 2-m temperatures are found inland at the locations of Skalholt and Kalfholl. A detailed comparison of the USGS land-use dataset and official maps of the area reveals that the land use contains too large water bodies or a too high a percentage of wetlands. The two mentioned stations are actually situated over water bodies in the model, while in reality they are only close to these. An additional simulation of case 1 in which all inland water bodies in the south of Iceland were removed

yielded a temperature increase of some 2–4 K at the aforementioned stations during daytime, even giving an overestimated temperature at some instances using an FDDA-all setup. The effect of this land-use modification was, however, very local and its impact on the general flow field was negligible. This nevertheless underlines the sensitivity of the local boundary layer temperatures to the underlying surface. This may seem obvious, but ever since the publication of Einarsson (1971), there has been consensus that temperatures in Iceland are governed by synoptic-scale advection and not local heat fluxes. Thus, future simulations of the local weather in the area could most likely benefit from a new and updated land-use dataset. Implementing such a dataset would, however, be a study in its own right and is therefore considered beyond the scope of the present study.

A clear advantage of the UAS system over for example AWSs is that it provides observations not only from near the surface, but also from an atmospheric column farther aloft. Thereby, one can avoid several issues

connected to the assimilation of only surface temperature observations, which are known to be especially problematic (e.g., Reen and Stauffer 2010). One such issue is connected to the surface heat flux, as its sign can change if the surface temperature is slightly increased by nudging the model toward observed surface temperatures. Such a switch in sign may lead to a drastic reduction in the boundary layer height. It is also well known that the assimilation of surface temperature observations can lead to an erroneous spread of temperatures not representative for the whole vertical extension of the ABL, as in the presence of a strongly stably stratified surface layer during nighttime or a superadiabatic surface layer during daytime (e.g., Stauffer and Seaman 1990). Solutions of various degrees of complication to these problems have been proposed. The switch in the surface heat flux can be avoided by also nudging the soil temperature (e.g., Reen and Stauffer 2010) and by making adjustments to the surface sensible and latent heat fluxes (Alapaty et al. 2001). Nudging a shallower layer when there are inversions and the whole ABL during events of free convection can mitigate the problem connected to strong temperature gradients near the surface. Nevertheless, these techniques are not optimal solutions and frequent profile observations as those provided by the UAS SUMO have the potential of avoiding the need to use them.

The inland penetration of the two investigated sea breezes was in this study deduced by manually investigating the AWS observations and corresponding model point estimations and horizontal fields. Future studies, including more cases and experiments, could benefit from a more statistical approach, as the objective technique proposed by Case et al. (2004).

The presented combination of WRF-FDDA and data acquired with a UAS is not limited to sea-breeze studies, but is likely to have a wide range of future applications. One example application in which one needs accurate high-resolution simulations and observations is investigations of flow in connection to existing and future wind farms. A related system is already proposed by Liu et al. (2011), where observations are combined with very high-resolution LES simulations using FDDA. The UAS SUMO would be an ideal tool for the verification and provision of atmospheric data for assimilation in such a system. SUMO has already been utilized to measure atmospheric turbulence in and around a small wind farm in Denmark, during spring 2011, as an integral part of the joint research project Autonomous Aerial Sensors for Wind Power Meteorology (Giebel et al. 2012; Reuder et al. 2012b).

Another potential future application for the SUMO-WRF-FDDA system is weather nowcasts or forecasts

for search and rescue (SAR) missions, as proposed by Rögnvaldsson (2011). Such missions depend critically on accurate weather information, both as the safety of the field personnel must be secured and as the missions must be run as efficiently as possible. Rescue missions often take place in remote areas or regions severely affected by natural catastrophes. For the provision of in situ meteorological data from the affected area, UAS represents a unique tool that can provide in situ data from such regions where conventional instrument platforms may not be applicable and manned flights too dangerous. An example of another modeling system for emergency response applications is that by Warner et al. (2004).

6. Summary and conclusions

Two summertime situations with northeasterly synoptic flow in southwest Iceland have been explored with a network of AWSs and the UAS SUMO.

Both flow situations are characterized by strong diurnal variation in boundary layer temperatures leading to thermally driven winds, predominantly in the form of sea-breeze circulation along the coast. These winds are to some extent reproduced by numerical downscaling of a state-of-the-art ECMWF operational analysis using the WRF model. However, by assimilating profile data from the UAS measured at Eyrarbakki in southwest Iceland using the FDDA technique, substantial improvements of wind, temperature, and humidity in the region are achieved.

The southwest Iceland sea breeze of 19 July 2009 penetrates about 40 km inland and reaches 250–300-m height at the coast. On this day, a modification of the thermal low over southwest Iceland generated through the assimilation of data from the UAS SUMO contributes to enhanced northerly flow at the west coast of Iceland, north of Reykjavik City. Thus, the penetration of cold and humid maritime air toward the city is inhibited and temperatures remain 6–8 K higher than in the simulation without the UAS data assimilated.

This study furthermore shows that accurate simulations of coastal weather at high latitudes are very dependent on a correct description of the boundary layer.

Envisioned future applications of the presented UAS SUMO and WRF-FDDA system include wind energy (e.g., siting for wind farms and intra-wind-farm measurements and simulations) and the improvement of local-scale nowcasts and forecasts for search and rescue missions.

REFERENCES

Alapaty, K., N. L. Seaman, N. S. Devdutta, and A. F. Hanna, 2001: Assimilating surface data to improve the accuracy of atmospheric boundary layer simulations. *J. Appl. Meteor.,* **40,** 2068–2082.

Anthes, R., 1974: Data assimilation and initialization of hurricane prediction models. *J. Atmos. Sci.,* **31,** 702–718.

Brisset, P., A. Drouin, M. Gorraz, P.-S. Huard, and J. Tyler, 2006: The Paparazzi Solution. ENAC, Toulouse, France, 15 pp. [Available online at http://www.recherche.enac.fr/paparazzi/papers_2006/mav06_paparazzi.pdf.]

Bromwich, D. H., L. Bai, and G. G. Bjarnason, 2005: High-resolution regional climate simulations over Iceland using Polar MM5. *Mon. Wea. Rev.,* **133,** 3527–3547.

Case, J. L., J. Manobianco, J. E. Lane, C. D. Immer, and F. J. Merceret, 2004: An objective technique for verifying sea breezes in high-resolution numerical weather prediction models. *Wea. Forecasting,* **19,** 690–705.

Chen, F., and J. Dudhia, 2001: Coupling an advanced land surface-hydrology model with the Penn State-NCAR MM5 modeling system. Part I: Model implementation and sensitivity. *Mon. Wea. Rev.,* **129,** 569–585.

Curry, J. A., J. Maslanik, G. Holland, and J. Pinto, 2004: Applications of aerosondes in the Arctic. *Bull. Amer. Meteor. Soc.,* **85,** 1855–1861.

Dudhia, J., 1989: Numerical study of convection observed during the winter monsoon experiment using a mesoscale two-dimensional model. *J. Atmos. Sci.,* **46,** 3077–3107.

Einarsson, M. A., 1971: *Meteorology* (in Icelandic). Idunn Publishers, 99 pp.

Fast, J. D., 1995: Mesoscale modeling and four-dimensional data assimilation in areas of highly complex terrain. *J. Appl. Meteor.,* **34,** 2762–2782.

Fuentes, M., L. Chen, J. M. Davis, and G. M. Lackmann, 2005: Modeling and predicting complex space-time structures and patterns of coastal wind fields. *Environmetrics,* **16,** 449–464.

Gahmberg, M., H. Savijärvi, and M. Leskinen, 2010: The influence of synoptic scale flow on sea breeze induced surface winds and calm zones. *Tellus,* **62A,** 209–217.

Giebel, G., S. U. Paulsen, J. Bange, A. la Cour-Harbo, J. Reuder, S. Mayer, A. van den Kroonenberg, and J. Mølgaard, 2012: Autonomous aerial sensors for wind power meteorology—A preproject. Rep. R-1798(EN), Risø DTU, 90 pp. [Available online at http://orbit.dtu.dk/fedora/objects/orbit:110631/datastreams/file_7726678/content.]

Grønås, S., and A. D. Sandvik, 1998: Numerical simulations of sea and land breezes at high latitudes. *Tellus,* **50A,** 468–489.

Hong, S.-Y., Y. Noh, and J. Dudhia, 2006: A new vertical diffusion package with an explicit treatment of entrainment process. *Mon. Wea. Rev.,* **134,** 2318–2341.

Jonassen, M. O., 2008: The Small Unmanned Meteorological Observer (SUMO)—Characerization and test of a new measurement system for atmospheric boundary layer research. M.S. thesis, Geophysical Institute, University of Bergen, Bergen, Norway, 125 pp. [Available online at http://web.gfi.uib.no/forskning/Master/Master_Jonassen.pdf.]

Jónsson, T., 2002: A brief investigation of diurnal variation of wind speed and wind directions in June (in Icelandic). Veðurstofa Íslands (Icelandic Meteorological Office), Tech. Rep. 02030, 12 pp.

Konrad, T., M. Hill, J. Rowland, and J. H. Meyer, 1970: A small, radio-controlled aircraft as a platform for meteorological sensors. *Appl. Phys. Lab. Tech. Dig.,* **11,** 11–19.

Langland, R. H., and Coauthors, 1999: The North Pacific Experiment (NORPEX-98): Targeted observations for improved North American weather forecasts. *Bull. Amer. Meteor. Soc.,* **80,** 1363–1384.

Liu, Y., A. Bourgeois, T. Warner, S. Swerdin, and J. Hacker, 2005: Implementation of observation-nudging based FDDA into WRF for supporting ATEC test operations. *Proc. Sixth WRF/15th MM5 Users Workshop,* Boulder, CO, NCAR, 1–4.

——, and Coauthors, 2011: Simultaneous nested modeling from the synoptic to the LES scale for wind energy applications. *J. Wind Eng. Ind. Aerodyn.,* **99,** 308–319.

Martin, S., J. Bange, and F. Beyrich, 2010: Meteorological profiling of the lower troposphere using the research UAV "M²AV Carolo." *Atmos. Meas. Tech. Discuss.,* **3,** 5179–5209, doi:10.5194/amtd-3-5179-2010.

Mayer, S., A. Sandvik, M. O. Jonassen, and J. Reuder, 2010: Atmospheric profiling with the UAS SUMO: A new perspective for the evaluation of fine-scale atmospheric models. *Meteor. Atmos. Phys.,* **116,** 15–26, doi:10.1007/s00703-010-0063-2.

——, G. Hattenberger, P. Brisset, M. O. Jonassen, and J. Reuder, 2012: A 'no-flow-sensor' wind estimation algorithm for Unmanned Aerial Systems. *Int. J. Micro Air Vehicles,* **4,** 15–29.

Mlawer, E. J., S. J. Taubman, P. D. Brown, M. J. Iacono, and S. A. Clough, 1997: Radiative transfer for inhomogeneous atmospheres: RRTM, a validated correlated-k model for the longwave. *J. Geophys. Res.,* **102** (D14), 16 663–16 682.

Nance, L. B., and D. R. Durran, 1997: A modeling study of nonstationary trapped mountain lee waves. Part I: Mean-flow variability. *J. Atmos. Sci.,* **54,** 2275–2291.

Otkin, J. A., D. C. Hartung, D. D. Turner, R. A. Petersen, W. F. Feltz, and E. Janzon, 2011: Assimilation of surface-based boundary layer profiler observations during a cool-season weather event using an Observing System Simulation Experiment. Part I: Analysis impact. *Mon. Wea. Rev.,* **139,** 2309–2326.

Pielke, R. A., 1974: A three-dimensional numerical model of the sea breezes over South Florida. *Mon. Wea. Rev.,* **102,** 115–139.

——, 2002: *Mesoscale Meteorological Modeling.* 2nd ed. Academic Press, 676 pp.

Pleim, J. E., and A. Xiu, 1995: Development and testing of a surface flux and planetary boundary layer model for application in mesoscale models. *J. Appl. Meteor.,* **34,** 16–31.

Reen, B. P., and D. R. Stauffer, 2010: Data assimilation strategies in the planetary boundary layer. *Bound.-Layer Meteor.,* **137,** 237–269.

Reuder, J., P. Brisset, M. O. Jonassen, M. Müller, and S. Mayer, 2009: The Small Unmanned Meteorological Observer (SUMO): A new tool for atmospheric boundary layer research. *Meteor. Z.,* **18,** 141–147.

——, and Coauthors, 2012a: FLOHOF 2007: An overview of the mesoscale meteorological field campaign at Hofsjökull, Central Iceland. *Meteor. Atmos. Phys.,* **116,** 1–13, doi:10.1007/s00703-010-0118-4.

——, M. O. Jonassen, and H. Ólafsson, 2012b: The Small Unmanned Meteorological Observer SUMO: Recent developments

and applications of a micro-UAS for atmospheric boundary layer research. *Acta Geophys.,* **60,** 1454–1473, doi:10.2478/s11600-012-0042-8.

Rögnvaldsson, O., 2011: Search and rescue software: Weather prediction system assists huminatarian aid. *Meteor. Technol. Int.,* 76–78. [Available online at http://www.scribd.com/doc/91499670/MeteorologicalTechnologyInternational-Sept2011.]

——, H. Ágústsson, E. M. Einarson, H. Ólafsson, H. Björnsson, and O. G. B. Sveinsson, cited 2007: Status report for year one of the RAV project (In Icelandic). [Available online at http://thjarkur.orkugardur.is/wordpress/wp-content/uploads/RAVarsskyrsla2007.pdf.]

Schroeder, A. J., D. R. Stauffer, N. L. Seaman, A. Deng, A. M. Gibbs, G. K. Hunter, and G. S. Young, 2006: An automated high-resolution, rapidly relocatable meteorological now-casting and prediction system. *Mon. Wea. Rev.,* **134,** 1237–1265.

Skamarock, W. C., and Coauthors, 2008: A description of the Advanced Research WRF Version 3. NCAR Tech. Note TN-475+STR, 125 pp.

Soler, M. R., R. Arasa, M. Merino, and M. Olid, 2011: Modelling local sea-breeze flow and associated dispersion patterns over a coastal area in North-East Spain: A case study. *Bound.-Layer Meteor.,* **140,** 37–56.

Stauffer, D. R., and N. L. Seaman, 1990: Use of four-dimensional data assimilation in a limited-area mesoscale model. Part I: Experiments with synoptic-scale data. *Mon. Wea. Rev.,* **118,** 1250–1277.

——, and ——, 1994: Multiscale four-dimensional data assimilation. *J. Appl. Meteor.,* **33,** 416–434.

——, ——, and F. S. Binkowski, 1991: Use of four-dimensional data assimilation in a limited-area mesoscale model. Part II: Effects of data assimilation within the planetary boundary layer. *Mon. Wea. Rev.,* **119,** 734–754.

Stull, R. B., 1988: *An Introduction to Boundary Layer Meteorology.* Kluwer Academic Publishers, 666 pp.

Teixeira, J., and Coauthors, 2008: Parameterization of the atmospheric boundary layer: A view from just above the inversion. *Bull. Amer. Meteor. Soc.,* **89,** 453–458.

Van den Kroonenberg, A., T. Martin, M. Buschmann, P. Bange, and J. Vörsmann, 2008: Measuring the wind vector using the autonomous Mini Aerial Vehicle M2AV. *J. Atmos. Oceanic Technol.,* **25,** 1969–1982.

Warner, T. T., R. A. Anthes, and A. L. McNab, 1978: Numerical simulations with a three-dimensional mesoscale model. *Mon. Wea. Rev.,* **106,** 1079–1099.

——, J. F. Bowers, S. P. Swerdlin, and B. A. Beitler, 2004: A rapidly deployable operational mesoscale modeling system for emergency-response applications. *Bull. Amer. Meteor. Soc.,* **85,** 709–716.

Xu, M., Y. Liu, C. A. Davis, and T. T. Warner, 2002: Sensitivity study on nudging parameters for a mesoscale FDDA system. Preprints, *19th Conf. on Weather Analysis and Forecasting/15th Conf. on Numerical Weather Prediction,* San Antonio, TX, Amer. Meteor. Soc., 4B.4. [Available online at https://ams.confex.com/ams/SLS_WAF_NWP/techprogram/paper_47401.htm.]